LITHOSPHERIC STRUCTURE ACROSS THE NORTHERN CANADIAN CORDILLERA FROM TELESEISMIC RECEIVER FUNCTIONS

Submitted by: Azadeh Ashoori Pareshkoohi

Thesis presented to the Faculty of Graduate and Postdoctoral Studies in partial fulfillment of the requirements for the degree of Master of Science in Earth Sciences

Department of Earth and Environmental Sciences

Faculty of Science

University of Ottawa

Supervisor:
Dr. Pascal Audet (Department of Earth and Environmental Sciences)

Thesis Committee:

Dr. Claire Samson, Carleton University

Dr. Glenn Milne, University of Ottawa

TABLE OF CONTENT

PREFACE

This thesis is formatted as a journal article. To comply with the regulations of the Faculty of Graduate and Postdoctoral Studies at the University of Ottawa, the thesis also contains an introductory chapter as well as a general synthesis and conclusion.

ABSTRACT

A major change in seismic velocities between Earth's crust and mantle is known as the Mohorovicic discontinuity (Moho). The depth of the Moho plays an important role in characterizing the overall structure of the crust and can be related to the tectonic setting of a region. Teleseismic P-wave receiver function techniques can provide estimates of the depth of the Moho and therefore crustal thickness under a broadband station. In this research we are interested in the structure of the crust and mantle across the northern Canadian cordillera, described by various tectonic settings. The teleseismic data recorded by broadband three-component seismic stations are used to perform receiver function analysis to determine the lateral variations of Moho depth under northern Canadian cordillera and map out the crustal thickness under the broadband stations. Based on visual inspection of receiver function results in the region, we find evidence of anisotropy or dipping reflectors in the crustal structure of the northern cordillera observed in back-azimuthal variations of transverse component receiver functions. We further provide a quantitative interpretation of receiver function in terms of anisotropy or dipping structure by decomposing the azimuthal variations of depth migrated receiver functions into back-azimuthal harmonics. This technique can be used to map out the orientation of anisotropy that may be related to cracks and/or rock texture caused by deformation. We resolve the Moho at an average depth of ~35 km along the western profile of the study area. Harmonic decomposition along the study area yields crustal anisotropy at depth 5-20 km, which does not extend in the lower crust. This can be the result of complex deformation at a detachment zone like a quasi-rigid displacement of the upper crust over a lower crust. The detected anisotropy over the study area is not coherent as the slow symmetry directions detected by harmonic decomposition are highly variable.

ACKNOWLEDGEMENTS

I would like to express my sincere gratitude to my supervisor Dr. Pascal Audet for his time, patience and all helps.

“Let it all go. See what stays”

LIST OF FIGURES

Chapter 1. Introduction

Chapter 2. Article

LIST OF TABLES

Chapter 1. Introduction

Chapter 2. Article

1. INTRODUCTION

1.1 Overview of geology

The Canadian Cordillera is a Phanerozoic mountain belt that extends from the Canada - US border in the south to the Beaufort Sea and Alaska in the north (Hyndman et al., 2005) is part of a vast mountain chain, called the North American Cordillera or Pacific Cordillera, extending from the southern border of US and Mexico to the U. S. state of Alaska. Although the Cordillera has similar physiography along its length, there are different tectonic regimes acting on this area mainly due to variations in plate tectonic interactions at its western margin (Hyndman et al., 2005). The origin of the Canadian Cordillera extends back to around 750 Ma. The late Neoproterozoic – earliest Cambrian break-up of Rodinia (between 750-540 Ma) led to the opening of a new ocean basin that was the distant ancestor of the present Pacific Ocean basin and to the formation of a continent-ocean boundary that is preserved today within the eastern Canadian Cordillera (Monger and Price, 2002). Collision of the margin of the old and stable North American continental plate with the oceanic lithosphere in the west played a key role in the prolonged evolution of the Canadian Cordillera (Monger and Price, 2002). This broad plate boundary zone has accommodated relative motion between the core of the North America plate and various oceanic plates over more than 200 Myr (Mazzotti et al., 2008). Terrane accretion, northward translation, and deformation continue to the present (Mazzotti et al., 2008). According to GPS (Global Positioning System) data in southwestern Yukon, the Yakutat block has a significant velocity relative to both the Pacific and the North American plates, resulting from the interaction of the Yakutat block with the North American plate along the Fairweather-Queen Charlotte Fault, which has contributed to the building of the tallest mountains in North America (Fairweather and St-Elias-Chugach Mountains) (Mazzotti et al., 2008). The strike-slip displacement of accreted terranes relative to North America along major faults such as the Tintina Fault, a dextral strike-slip fault with about 425 km of Paleogene displacement, played a major role in the development of the northern Canadian Cordillera (Zelt et al., 2006).

Today, five northwesterly trending geomorphological belts (see Figure 1-1), defined on the basis of their geological histories, structural style, and rock types (see table 1-1) are making the Canadian Cordillera (Monger et al., 1982). These five geomorphological belts from east to west of the Canadian Cordillera are named the Foreland, Omineca, Intermontane, Coast, and Insular belts (Monger and Price, 2002). The characteristics involved in this division are landforms, rock types, metamorphic grade and structural style (Gabrielse et al., 1991; Monger and Price, 2002).

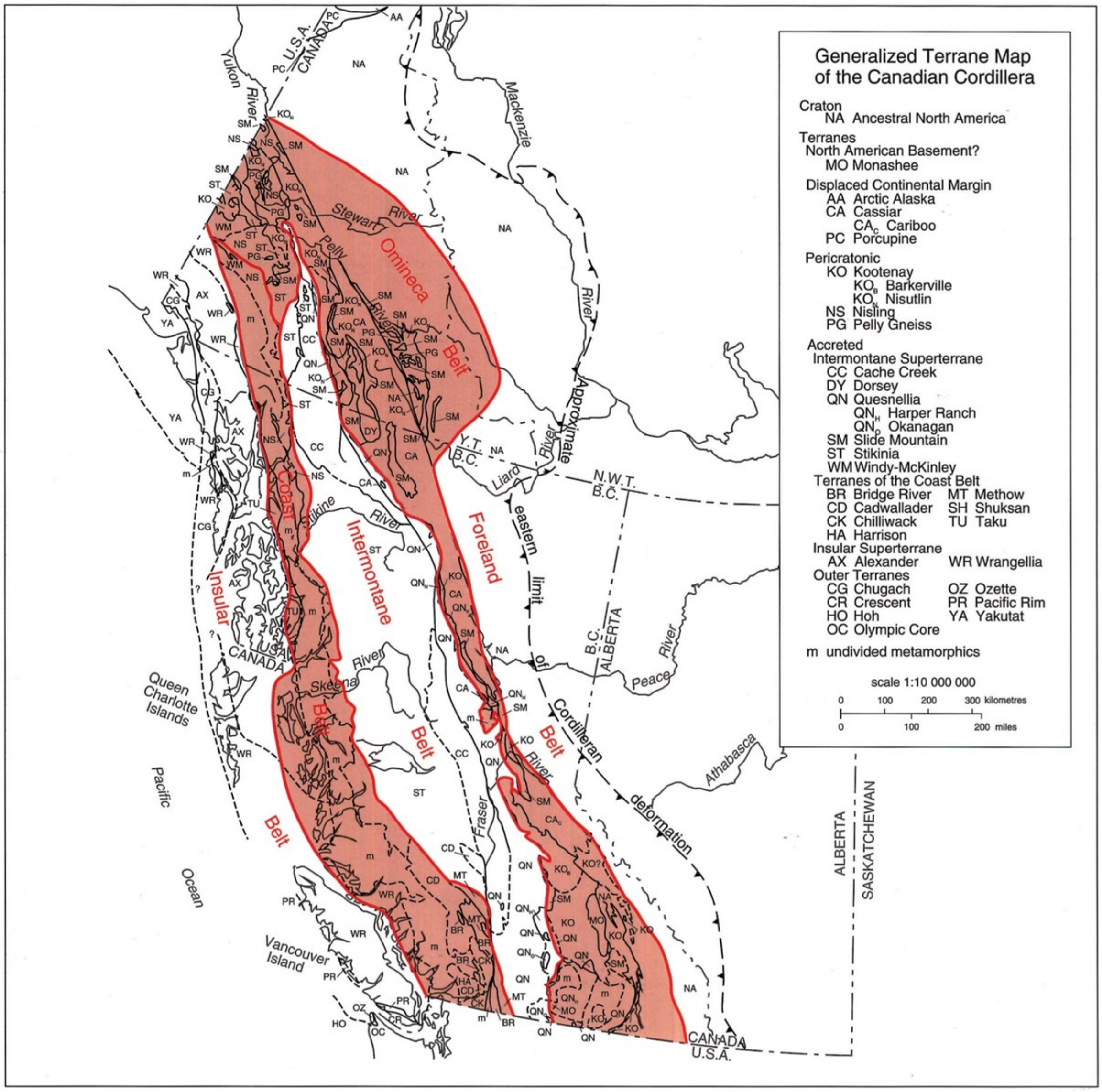

Figure 1-1: Simplified terrane map of Canadian Cordillera (Gabrielse and Yorath, 1989; Wheeler et al., 1991)

Table 1-1: Morphogeological belts of the Canadian Cordillera (Monger and Price, 2002)

Belt	**Physiographic units**	**Geology**
Foreland Belt	Rocky, Mackenzie, and Franklin mountains	Mainly sedimentary rock
Omineca Belt	Purcell, Selkirk, Monashee, Cariboo, Omineca, Cassiar and Selwyn mountains	Sedimentary, volcanic and granitic rock, typically metamorphosed up to high grades
Intermontane Belt	Interior, Stikine, and Yukon plateaus and Skeena Mountains	Volcanic, sedimentary, and granitic rocks
Coast Belt	Coast and Cascade mountains	Mainly granitic rock
Insular Belt	Insular Mountains, Saint Elias Ranges, coastal depressions, continental shelf and slope	Volcanic, sedimentary, and granitic rocks

An interpreted profile through the crust and uppermost mantle in the northern Cordillera is shown in Figure 1-2. This is the result of downward extrapolating of surface geology data in combination with Lithoprobe seismic reflection and refraction profile results (Clowes et al., 1995; Clowes and Hammer, 2000; Monger and Price, 2002).

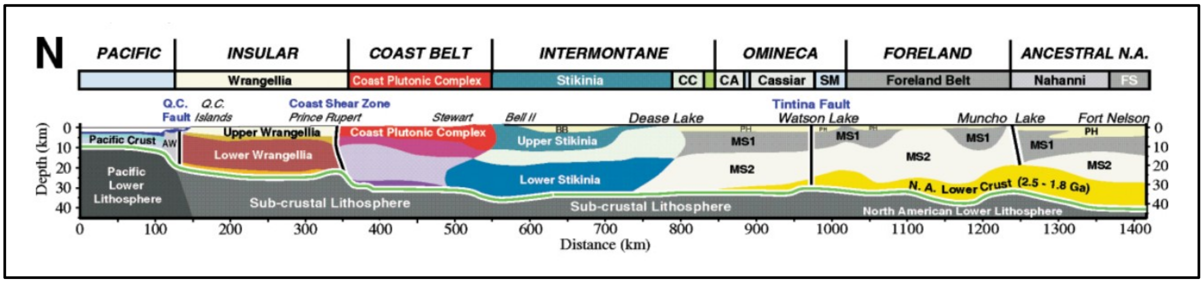

Figure 1-2: Interpreted simplified lithospheric structures along the northern Cordilleran Lithoprobe transect. The green line is the crust-mantle boundary (Moho). AW: accreted wedge; AX: Alexander terrane; BB: Bowser Basin; CA: Cassiar terrane; CC: Cache Creek terrane; CD: Cadwallader terrane; FS: Fort Simpson (a Precambrian terrane in the craton); KO: Kootenay terrane; MS1: undivided Precambrian (1200-800 Ma) metasedimentary rocks; MS2: undivided Precambrian (1800-1200 Ma) metasedimentary rocks; MT-SH: undivided Methow and Shuksan terranes; QN: Quesnel terrane; SM: Slide Mountain terrane; ST: Stikine terrane; WR: Wrangellia. Figure modified by P.T.S. Hammer from Clowes and Hammer (2000), and Monger and Price (2002). Vertical exaggeration 2.7:1

A combination of tectonic processes has contributed in shaping the Cordillera since the late Neoproterozoic (750 Ma). Each belt has recorded the formation of structures during Middle Jurassic through early Tertiary mountain building episodes, containing compressional deformation between ~185-60 Ma followed by extensional deformation between ~59-40 Ma (Monger and Price, 2002). Although the physiography in this region matches closely to the bedrock geology, it is not perfect due to late Tertiary and Quaternary (~≤20 Ma) differential vertical movements (Monger and Price, 2002).

1.2 Receiver functions

An earthquake occurs because of the motion on a segment of a fault; this fault rupture produces elastic vibrations called seismic waves, which propagate into the Earth. The generated seismic waves are divided into two types based on their form of travel; body waves travel through the interior of the Earth and surface waves travel along the surface of the Earth. A teleseismic wave is an earthquake wave that occurs at an epicentral distance further than about 30° away from the receiver that can be approximated by a plane wave arriving almost vertically beneath the seismic station.

The velocity of the propagating waves through a medium depends on its physical properties; the wave responds to changes in physical properties such as density and elastic moduli, making them useful to study the interior of the earth. Seismic body waves from distant events carry information about the source, the path of the wave and the lithospheric and crustal structure near the receiver. To extract information about the structure near the receiver, one common method, called receiver functions, studies S waves generated by P-waves converted at a discontinuity in seismic velocity. The receiver function technique is a method based on deconvolution analysis to remove the signal related to the source and the propagation path in order to recover the crustal structure beneath the seismic station (e.g. Burdick and Langston, 1977; Langston, 1977; Dueker and Sheehan, 1997; Bianchi et al., 2010). Teleseismic receiver functions are used to study Moho depths in subduction zones and other complex settings (e.g. Langston, 1989; Ammon and Zandt, 1993; Zhu and Kanamori, 2000; Rondenay et al., 2001; Nabelek et al., 2009; Frassetto et al., 2011).

The basic aspect of this method is that some portion of the incident P wave energy from a teleseismic event will be converted to an S wave (Ps) at significant and relatively sharp velocity discontinuities (e.g., the Moho), and arrive at the station within the P wave coda (Galetti and Curtis, 2012). The amplitude, arrival time, and polarity of the locally generated

Ps phases are mainly sensitive to the S-velocity structure beneath the recording station. For events more than 30° of epicentral distance, P waves are steeply incident and dominate the vertical component of ground motion, whereas Ps are mostly contained on the horizontal components of ground motion. In other words, source and path effects are mostly recorded by the vertical component of the seismograms; accordingly a deconvolution of the vertical from the horizontal components produces time series (i.e., receiver functions) that contain the P to S converted waves related to the structures beneath the station (Vinnik, 1977; Langston, 1979; Levin and Park, 1998; Savage, 1998). By measuring the time difference in arrival of the converted Ps phase relative to the direct P wave, the depth of the discontinuity can be estimated using a reference velocity model (e.g. Ammon, 1991; Levin and Park, 1997; Shiomi and Park, 2008).

Figure 1-3 shows a schematic teleseismic earthquake signal arriving at a seismic station illustrating the different phases. The first letter P denotes a direct, plane P wave incident from below and the other letters denote the travel paths in the crust of the scattered waves. The subsequent upper case letters denote down-going paths, and the lower case letters denote up-going paths, and m indicates conversion from the Moho interface.

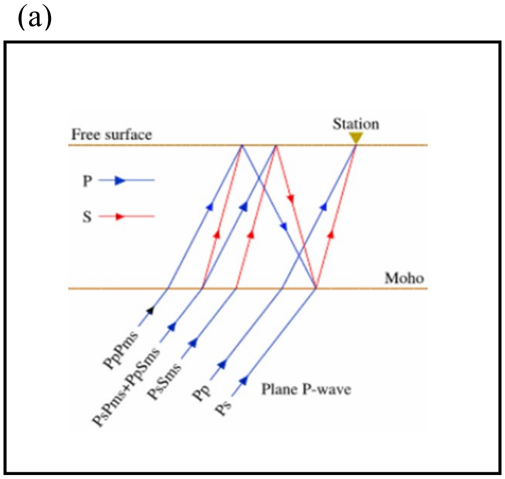

Figure 1-3: (a) Simplified ray diagram showing the major P to S converted phases for a single layer over a half-space. (b) The corresponding simplified receiver function showing the converted P waves at layer over a half-space.

The principle of receiver functions is based on two main assumptions. First, the teleseismic P wave acts like a plane wave that is converted to an S wave at a discontinuity. Second, the vertical component of the seismograms records the effects of source and path. Therefore, by deconvolving the horizontal components from the verticals radial and transverse time series are obtained (Bianchi et al., 2010). The radial component of the receiver function (shear wave polarized in the vertical plane between source and receiver) usually contains the energy mostly from the isotropic subsurface seismic structure, while the transverse component (shear wave polarized horizontally along the path) usually carries energy related to the anisotropic and/or dipping seismic structure beneath the station (Ferris et al., 2003; Bannister et al., 2007; Kawakatsu and Watada, 2007; Agostinetti et al., 2009; Nikulin et al., 2009; Bianchi et al., 2010). Harmonics analysis, based on variations in the amplitude of both radial and transverse receiver function components as a function of the back-azimuth of the incident waves, can be used to identify anisotropy in the subsurface (Savage, 1998; Park et al., 2004; Piana Agostinetti et al., 2008b; Bianchi et al., 2010).

1.3 Seismic anisotropy

A medium is anisotropic when the value of a vector property at a point in that medium varies with direction. Thus, there is a difference between anisotropy and heterogeneity, which is the variation in scalar or vectorial values between two or more points. Seismic anisotropy can be defined as the "dependence of seismic velocity upon angle" of wave propagation (Thomsen, 2002). Compressional and shear waves are the types of elastic waves propagating in isotropic elastic solids. Particle motion in the direction of propagation is the characteristic for compressional wave, whereas for a shear wave, the particle motion is in a plane normal to the direction of propagation. There is no pure compressional or transverse wave for anisotropic media except in certain directions. In this kind of media, particle motion contains a quasi-P wave and 2 quasi-S waves (Anderson, 1989). According to Hooke's Law, all six components of stress and strain in a solid medium, three extensional and three shear, are linearly related,

$$T_i = C_{ij} S_i$$

where, C_{ij} is an elastic constant expressing the proportionality between the stress, T_i, and strain, S_i. There are at most 21 elastic constants for the most un-symmetrical crystal, a triclinic crystal. For an isotropic solid the constants are independent of the choice of axes and reduce to two; these are the Lamé parameters λ and μ.

Tectonic forces are responsible for deformation in the crust and mantle and their internal structures, which results in the acquisition of a coherent rock fabric. This fabric gives rise to significant elastic anisotropy, and therefore seismic anisotropy. Uncovering the signature of rock fabric through the analysis of seismic anisotropy properties of rocks both in the crust and mantle provides important information regarding the stress regime and tectonic history of a given region. There are two principal mechanisms that can explain anisotropy in the crust and in the mantle. Shape-Preferred Orientation, SPO, and Lattice-Preferred Orientation, LPO, of earth material (e.g. Fouch and Rondenay, 2006; Bianchi, 2010). In general, SPO (structural features such as faults, regularly oriented cracks or layering) can be the effective mechanism for the development of seismic anisotropy in the earth's crust. LPO develops when stresses applied to a rock produce the alignment of anisotropic mineral, such as micas (in the crust) and olivine (in the mantle). Both SPO and LPO (in general) can be modeled as a transversely isotropic material (or hexagonal symmetry), where physical properties are symmetric about an axis, normal to a plane of isotropy. This type of material gives rise to either a fast or slow axis of seismic wave propagation corresponding to the symmetry axis, and a slow or fast plane orthogonal to it.

1.4 Research purpose

The Earth's crust is known to be a very heterogeneous layer due to variations in chemical compositions and physical properties in both lateral and vertical directions. Knowledge of crustal structure is important in studies of bulk crustal composition and evolution, and in studies of the support of topography (i.e., isostasy). However, the crust can be highly heterogeneous and contain internal layering, such that the determination of its geometry and structure is challenging and the estimated parameters are highly uncertain.

Our goal in this thesis is to study the crustal structure across the northern Canadian Cordillera by using teleseismic receiver functions. These data allow us to probe the discontinuities in crust and mantle structure via their scattering (i.e., conversions, reflections) properties. Knowledge of crustal structure in this area will help refine tectonic models characterized by rapid deformation in order to understand processes associated with the formation and evolution of the northern Canadian Cordillera.

2. ARTICLE: LITHOSPHERIC STRUCTURE ACROSS THE NORTHERN CANADIAN CORDILLERA FROM TELESEISMIC RECEIVER FUNCTIONS

Azadeh Ashoori Pareshkoohi, Pascal Audet

Department of Earth and Environmental Sciences, University of Ottawa, Ottawa, Canada

2.1 Abstract

The composition and thickness of the crust and underlying mantle are important parameters that reflect the evolution and deformation of the lithosphere. In the northern Canadian Cordillera, these properties are poorly known due to sparse coverage of broadband seismic stations. In this work we characterize the structure of the crust and mantle across the northern Canadian Cordillera using data form a portable array of stations (CANOE array). The teleseismic data recorded by these broadband stations were used to perform receiver function analysis. These data indicate the presence of anisotropy or dipping reflectors in the crustal structure of the northern Cordillera observed in back-azimuthal variations of transverse component receiver functions. We provide a quantitative interpretation of receiver functions in terms of anisotropy or dipping structure by decomposing the azimuthal variations of depth migrated receiver functions into back-azimuthal harmonics. This technique can be used to map out the orientation of anisotropy that may be related to cracks and/or rock texture caused by deformation. We further show how crustal thickness varies along the array from the interior of the Cordillera to the adjacent Canadian Shield. These results show that crustal thickness is

between 30 and 35 km thick on average, supporting the thesis that the high-elevation Cordillera is isostatically supported by the thermal buoyancy of the hot underlying mantle.

2.2 Introduction

The northern Canadian Cordillera is one of the most seismically active regions in North America, yet the current tectonic models describing such deformation are poorly constrained. The current leading model (called the “orogenic float” model) proposes a thin rigid crustal layer, decoupled from the underlying weak lower crust and mantle due to elevated basal temperatures, which is pushed horizontally at the plate boundary to the west and transmits stresses throughout the Cordillera (Mazzotti and Hyndman, 2002). This model is at odds with the traditional isostatic models that require a thick crustal root supporting the high topography of the Cordillera. In contrast, the orogenic float model uses heat flow data to suggest very high temperatures in the upper mantle, thus providing thermal buoyancy to the Cordillera that supports the topography without requiring a thick crustal root. This hypothesis is generally supported by active source seismic studies that were carried out as part of Lithoprobe (e.g., Clowes et al., 1996; Perry et al., 2002; Cook et al., 2004). In general these studies indicate that the crust is ~35 km thick, but spatial coverage is very sparse. Increased coverage of broadband seismic stations is now allowing the mapping of crustal thickness over a large area.

One implication of the elevated temperature at the base of the crust is that lower crustal rocks must be very weak and therefore flow at very low shear stresses. This is supported by generally low values of the effective elastic thickness (<10 km) in the area (e.g., Flück et al., 2003; Audet et al., 2007), which indicate that only the upper crust can support tectonic stresses.

The consequence of a weak lower crust is to concentrate strain from plate boundary stresses; such a weak layer may then form a detachment zone that allows the upper crust to transmit stresses from the collision of the Yakutat block in the west to the Cordilleran Deformation Front to the east, thus explaining the occurrence of earthquakes at long distances from the plate boundary. A thin, weak lower crustal detachment (shear zone) imparts a mineral texture (or fabric) to the rocks, giving rise to elastic anisotropy. Such anisotropy can be deciphered using seismic analysis techniques; the presence or absence of the lower crustal detachment zone can thus be examined using seismic data. In this work we use scattered teleseismic waves (i.e., receiver functions) to study both the thickness and anisotropy of the crust in the northern Canadian Cordillera. We first review the geology and tectonic setting of the area, followed by a description of the methodology employed. We then present the results and discuss their implications for the orogenic float model.

2.3 Overview of geology, tectonics and crustal structures in Yukon region

The Canadian Cordillera, is only one segment of the circum-Pacific mountain belts (Monger & Price, 2002), and can be divided into five tectonic settings (Colpron et al., 2007).

1. Ancestral North America (Laurentia), including the Yukon-Tanana upland, Alaska Range, and Kootenay terrane—the autochthon and parauthochthon;
2. The allochthonous marginal pericratonic terranes (Intermontane terranes)—the peri-Laurentian realm;
3. The Insular and Northern Alaska terranes, which evolved in the Arctic realm in Paleozoic time;

4. Oceanic and accretionary complex terranes, which evolved alongside the Intermontane and Northern Alaska–Insular terranes;
5. Mesozoic and younger arc and accretionary terranes that form a western and southern fringe to the older elements;

Based on the relationship discussions by Colpron et al. (2007), the Intermontane terranes evolved together in the peri-Laurentian realm in mid- to late Paleozoic time as a set of offshore island arcs and continental fragments outboard of the Slide Mountain ocean basin that separated them from the Laurentian margin. Each terrane has the characteristics of the tectono-stratigraphic record of one or more depositional environments, which is the reason for the complexity of convergent plate margins (Colpron et al., 2007).

In Colpron et al.'s (2007) model of Cordilleran evolution, the northwestern Laurentia was the primary location for the generation of the Yukon-Tanana terrane (the underpinning of the Intermontane terranes). The terrane migrated towards south and west when the Slide Mountain Ocean opened in mid- to late Paleozoic time. When the Slide Mountain Ocean closed in the early Mesozoic, the Yukon-Tanana terrane rejoined to the Laurentian margin. The relative plate motions and oblique subduction within the Slide Mountain Ocean prior to their Jurassic accretion to North America accommodated the large-scale translation of the Intermontane terranes.

According to Zelt et al. (2006), in summarizing the tectonic settings of Canadian Cordillera, a series of passive margin miogeoclinal sequences formed to the west of the Nahanni terrane after the Palaeoproterozoic convergence episodes, as the results of lithospheric extension in a number of phases (e.g. Thompson et al., 1987; Thorkelson et al., 2001). The formation of the Foreland fold and trust belt of the easternmost Cordillera is the result of the accreting of the Intermontane super terrane to the North American plate during the Middle Jurassic. As a consequence of this collision, the passive margin sequences were folded, detached from crystalline basement, and trust on to the edge of proto-North America. The suture zone of this collision is present in the Omineca belt, west of the Foreland belt, and in the westernmost section of cratonic North America's migeocline. The Intermontane superterrane is a collage of terranes whose accretion caused Middle Jurassic deformation along the western margin of North America. Most of the eastern accreted terranes have been interpreted to be thin klippes occupying only a portion of the crust, thrust over a thick wedge of Precambrian meta-sediments of the ancient North American margin (Gabrielse 1985; Snyder et al., 2002). The accretion of Insular super terrane to North America occurred during the Late Cretaceous which caused deformation of the interior of the orogen and formation of the plutonic Coast belt. The major deformation and thermal events occurred during Eocene due to transcurrent motion between the oceanic and continental plates. The northward dextral motion of the terranes relative to North America is accommodated by strike-slip displacements continuing into the Cenozoic, though the amount of this dextral displacement throughout the Cordillera remains ongoing debate. The Tintina Fault, TF, is one of the most notable shear zones along the northern Canadian Cordillera which separates deformed autochthonous North American rocks from accreted rocks along its path. The TF joins the Northern Rocky Mountain Trench (NRMT) near the B.C./Yukon border and its length goes over 1900km with the NRMT. Our study area encompasses the Ancestral North America east of the Cordilleran deformation front and extends into the Intermontane belts to the west, therefore sampling a large portion of the tectonic terranes making up the northern Canadian Cordillera.

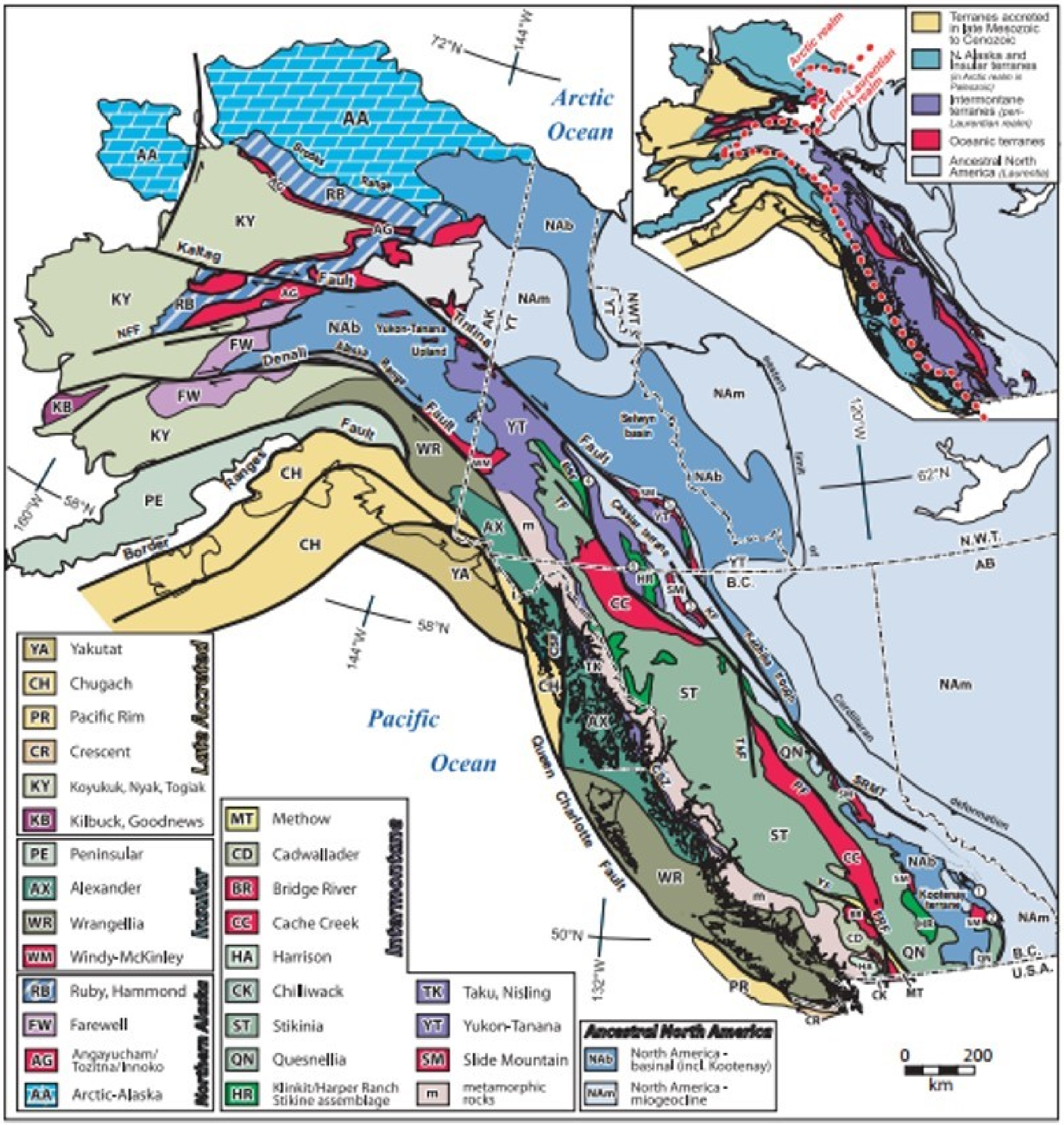

Figure 2-1: Terrane groupings and tectonic domains of the Canadian-Alaskan Cordillera (Colpron et al., 2007). Sources: Wheeler et al. (1991); Silberling et al. (1992); Colpron (2006). Abbreviations: BSF: Big Salmon fault; CSF: Chatham Strait fault; CSZ: Coast shear zone; FRF: Fraser River fault; KF: Kechika fault; NFF: Nixon Fork–Iditarod fault; PF: Pinchi fault; SRMT: southern Rocky Mountain trench; TkF: Takla-Finlay-Ingenika fault system; YK: Yalakom fault. AB: Alberta; AK: Alaska; B.C.: British Columbia; N.W.T.: Northwest Territories; YT: Yukon

2.4 Methodology

In earthquake-generated source techniques (i.e., passive techniques), the sensitivity of the results is based on the nature of the interactions between seismic waves and Earth structure, which can be transmission or scattering based interactions. Examples of transmission-based passive seismic techniques to image upper mantle structure include seismic tomography from the analysis of body-wave travel times or surface-wave dispersion, and shear wave splitting. In transmission-based methods the integrated effect of the seismic structure on a wave traveling from source to receiver is recorded, thus resolution is limited along the path of the traveling waves. On the other hand, the scattering-based methods deal with the interaction of seismic waves with small-scale structure such as discontinuous surfaces, or heterogeneities on a scale comparable to the wavelength of the seismic wave, that produce secondary phases. Scattering-based techniques are therefore better suited at characterizing the detailed isotropic and anisotropic structure of the crust (Frederiksen, 2000). Techniques using scattering of high-frequency P or S earthquake waves are able to construct high-resolution upper mantle images. Teleseismic receiver functions, which are source-normalized recordings of the P-coda (estimates of the Earth's Green's function) (Langston, 1979; Cassidy and Ellis, 1991), are the most common types of teleseismic scattering techniques (other examples include ScSp reverberations (e. g., Snoke et al., 1977; Nakanishi et al., 1981; Iidaka and Obara, 1993; Bourne and Stuart, 2000)). Receiver functions typically enable the reconstruction of one dimensional, isotropic Earth structure. However, sufficient coverage in back-azimuth and epicentral distance sampling allows these techniques to resolve anisotropic and dipping structures (e.g. Cassidy, 1992; Levin and Park, 1997; Bostock, 1998; Savage, 1998; Farra and Vinnik, 2000; Frederiksen and Bostock, 2000). In this section we discuss the requisite pre-processing procedures to achieve high-resolution receiver function data for the selected seismic stations across the northern Canadian Cordillera.

2.4.1 Data source and preparation

For this study we used 379 earthquake events with magnitude greater than 5.5 within the epicentral distance range 30º – 100º that occurred between January 2003 and December 2005, recorded by 19 broadband seismic stations of the network XN (CANOE), Figure 2-2. The geographical coordinates of individual stations are presented in Table 2-2. The epicentral distribution of the collected events at station A02 is shown in Figure 2-3 as an example.

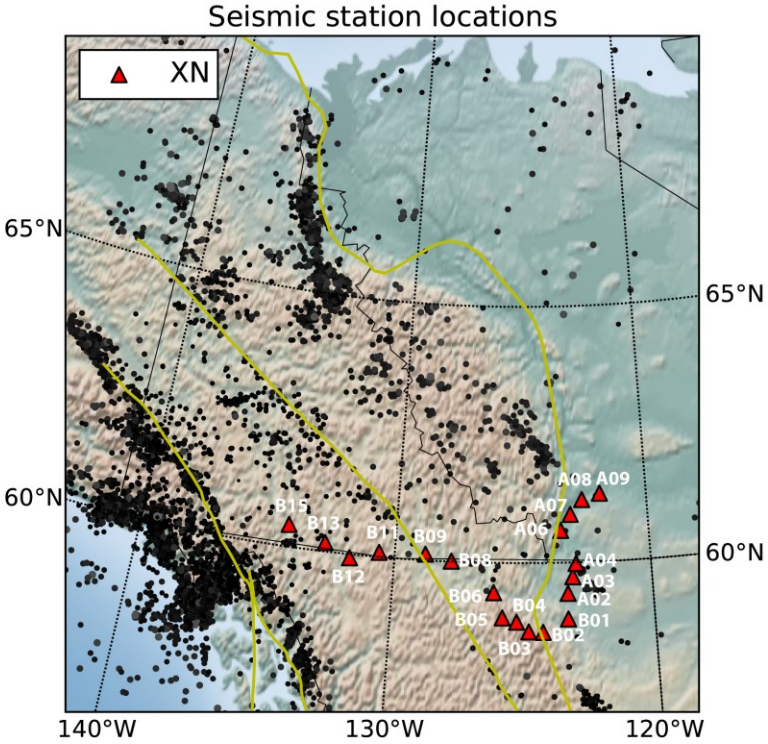

Figure 2-2: Map of the seismograph stations from the XN network (red triangles). Black circles are earthquakes recorded between 2000 and 2015. Yellow lines are major tectonic boundaries.

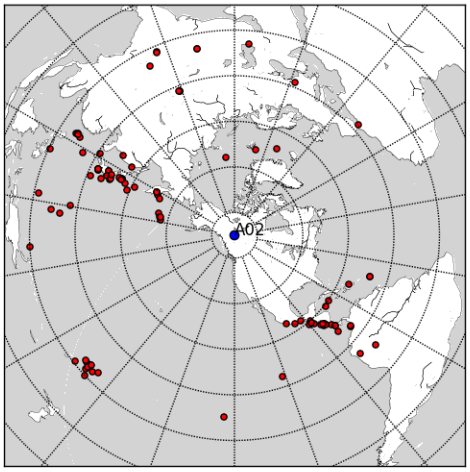

Figure 2-3: Epicenter distribution of the events with magnitude >5.5 (red circles) used to estimate P receiver functions at station A02.

2.4.2 Rotations

A three-component seismometer records ground motion along three orthogonal axes: North-South (N), East-West (E), and Vertical (Z), which are not necessarily aligned with the incoming direction of the earthquake waves; the direct and converted waves can therefore be resolved on all three components. A rotation of the coordinate system should be done to align the seismograms into the frame of reference defined by the direct P wave. For this study we first rotate the NEZ data into the vertical-radial-transverse (ZRT) coordinate system show in Figure 2-4(a). In this system, Z remains in the vertical direction but the two horizontal components are rotated into the radial R (waves polarized in the vertical plane connecting station and event) and tangential, or transverse, T (waves polarized in the direction normal to the vertical plane) components. The rotation is related to the angle between a vector pointing from the seismic station to the north and the vector pointing from the seismic station to the earthquake epicentre (back-azimuth angle). The vertical component contains most of the direct

P wave energy while most of the energy of converted P-to-S (Ps) wave is dominant on the R component.

The ZRT components are further rotated to align the seismograms into the P, S_V (shear radial) and S_H (shear transverse) components of motion (Sodoudi, 2005) (see Figure 2-4(b)). To carry out this operation, we require information on the slowness and some assumptions on the crustal velocity structure. We extract the P wave slowness from a global travel-time table based on the epicentral distance between source and receiver. We assume crustal P and S velocities (Vp and Vs) of 6 km/s and 3.6 km/s respectively. The direct P wave is isolated onto the P component of motion, whereas the S_V and S_H components contain information on the P-to-S converted waves. These seismograms still contain information on source and path effects, and this discussion leads naturally to deconvolution.

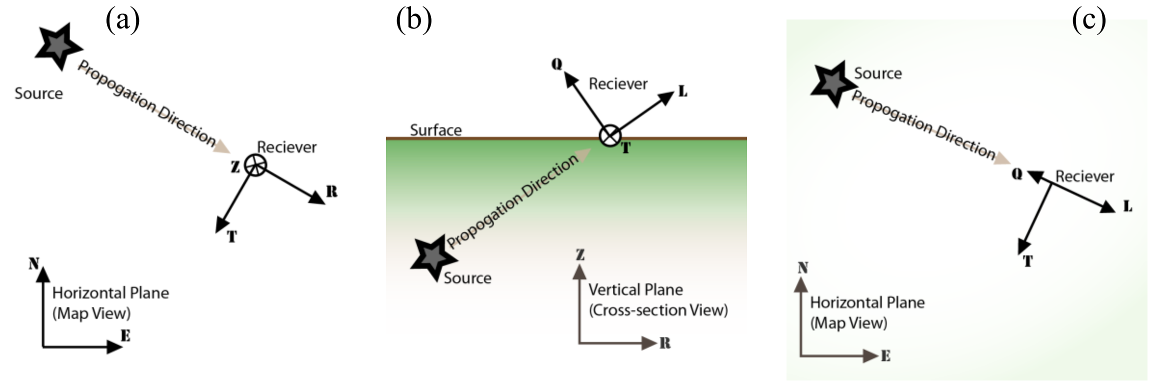

Figure 2-4: Illustration of rotation of coordinate systems for incoming events. (a) Rotation to ZRT. (b, c) Rotation to P-S_V-S_H (also called LQT). From IRIS (www.iris.edu).

2.4.3 Deconvolution

A receiver function is an approximation of the impulse response of the medium underlying the seismic station when excited by a seismic event. The source parameters have to be known to calculate the exact impulse response. In the absence of source information, we make the assumption that the P component of motion represents the source signature. Thus, we deconvolve the P component from the S_V and S_H components. The deconvolution can be made either in time domain or in frequency domain.

Water level deconvolution and damping factor deconvolution are two of the earliest-developed deconvolution techniques drawn directly from the work of the mathematician Norbert Wiener. Wiener deconvolution is a non-iterative, direct inverse technique that operates in the frequency domain to reduce the effect of noise in the deconvolution (Wiener, 1964). The filter applied is based on the mean power spectral density of the noise, which is assumed to be white Gaussian noise and independent of the input. The amplitude of the filter is inversely related to the signal-to-noise ratio (SNR) of the data, so when the SNR is very high (when there is little noise present in the data), the effect of the filter is weakened so the deconvolution is almost identical to a direct spectral division. The usual convolution model for ground displacement for an incident P wave with constant ray parameter at a single station is (Langston, 1979):

$$DP(t) = I(t) * S(t) * P(t)$$

$$DS_V(t) = I(t) * S(t) * S_V(t)$$

$$DS_H(t) = I(t) * S(t) * S_H(t),$$

where $DP(t)$, $DS_V(t)$, and $DS_H(t)$ represent respectively the recorded seismogram for compressional, shear radial (S_V), and shear transverse (S_H) component Green's functions; I(t) is the instrument response; and S(t) is the teleseismic source function. The most important assumption in receiver function technique is that the P component Green's function approximates a delta function, $P(t) \sim \delta(t)$, which means that converted phases on the P component of motion are considered negligible. Thus,

$$DP(t) = I(t) * S(t).$$

Moreover, assuming that instrument responses are matched between components, the source and deep mantle effect in the radial component can be removed by deconvolving the P component, DP(t), from the shear radial component, $DS_V(t)$ (Lin, 1995). The procedure for performing the deconvolution is to divide the spectrum of radial component by the vertical component in the frequency domain, e.g.,

$$S_V(\omega) = DS_V(\omega) / DP(\omega).$$

To reduce the effects of noise generated by dividing by very small numbers, a substitute water-level process is given by Dey-Sarkar and Wiggins (1976). In the water-level method the small values in the denominator are replaced with a fraction of the maximum value in the denominator. Replacing small values by larger ones reduces the effect of low-amplitude frequency coefficients on the receiver function and makes the process numerically more stable. Remembering that the inverse of a complex number z can be written as:

$$1/z = Z^* / ZZ^*,$$

where * indicates the complex conjugated, the receiver function can be rewritten as:

$$S_V(\omega) = DS_V(\omega)\, DP^*(\omega) / DP(\omega)\, DP^*(\omega) + \alpha,$$

where α is now called the water level. The inclusion of α is equivalent to adding white noise to the signal and effectively shifts the power spectrum of the denominator (the auto-correlation of the input) vertically (Lines and Treitel, 1984). It also broadens and boosts the height of the spectrum to increase the bandwidth. The filter is the inverse of the denominator, so in practice the addition of α enhances its effectiveness as a low pass filter. As α approaches zero, the above equation corresponds to pure spectral division. As α becomes large and approaches the maximum value of the original spectrum, the power spectrum flattens out and the denominator is approximately a constant value.

In standard wiener deconvolution, the noise spectrum is assumed to be Gaussian random noise with zero-mean (Wiener, 1964). For this study we use a modified Wiener deconvolution, where the regularization parameter is calculated from the pre-event co-variant noise spectrum between vertical and horizontal components to reduce contamination from seasonal noise that causes tilt effects (Audet, 2010). Single events can be processed individually according to this modified wiener spectral deconvolution and then stacked afterwards. To obtain a better visualization of the receiver function results, we used a second-order Butterworth filter with various corner frequencies (see next section); the filter with corner frequencies of 0.05-0.5 Hz provided the best resolution for these data.

Finally, following deconvolution and filtering, it is necessary to stack receiver functions from different epicentral distances at each station to increase the signal to noise ratio. Stacking the receiver functions (for Ps conversion phase) enhances the direct conversions, while the multiples are considerably weakened. To carry out this step we divided the globe into regular bins based on the slowness and the back-azimuths. Receiver functions were stacked into 7.5° back-azimuths (from 0° to 360°) and 0.002 s/km slowness bins (from 0.04 to 0.08 s/km).

The effects of four band pass filters with different high frequency corners on the resolution of the converted pulses are illustrated in Figure 2-5. The best signal to noise ratio is obtained using corner frequencies of 0.05-0.5 Hz. At low frequencies, the pulses are broad and do not resolve sharp Ps phase arrivals. At high frequencies, the receiver functions are noisier, mainly because the teleseismic P waves are attenuated at those frequencies and do not carry coherent energy. Results are shown in section 2.5.1.

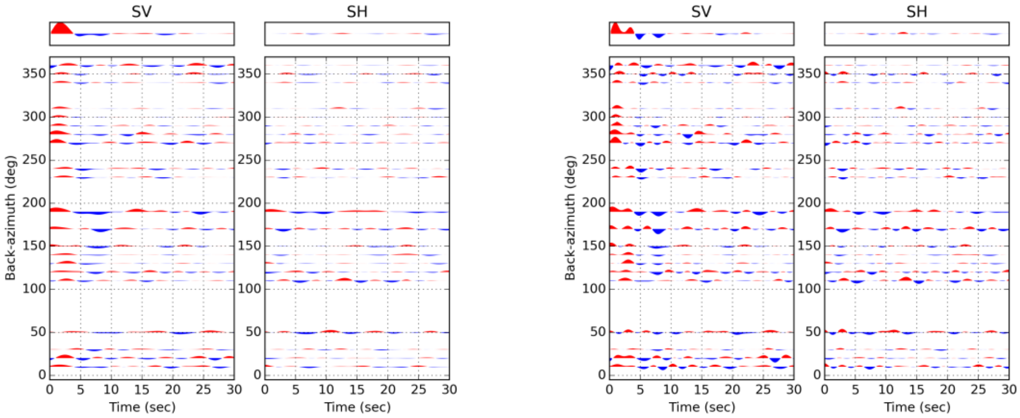

Filter 1: (0.05 – 0.25 Hz)

Filter 2: (0.05 – 0.35 Hz)

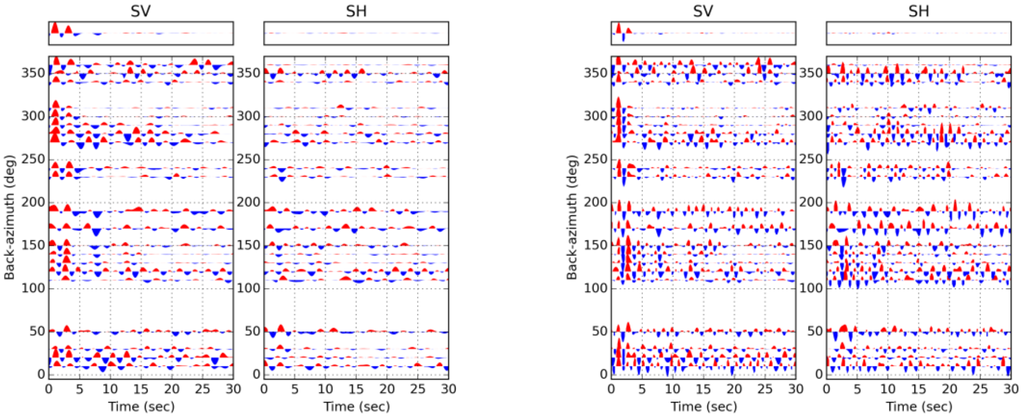

Filter 3: (0.05 – 0.5 Hz)

Filter 4: (0.05 – 0.8 Hz)

Figure 2-5: Receiver functions for station A02 obtained using four band pass filters with various high frequency corners. Radial (S_V) and transverse (S_H) receiver functions are sorted by back-azimuth of incoming wave. Low corner frequencies do not resolve sharp pulses in the receiver functions. A high corner frequency corner produces noisy signals.

2.4.4 Migration of receiver function

The primary results for the receiver functions are the time domain sections illustrating the converted phases at various back-azimuths. For results shown as a function of slowness, see Appendix A. The arrival time of the main positive Ps converted phase on the radial component is primarily an indication of Moho depth. In order to find the approximate depth of each Ps conversion, we apply a time-to-depth migration procedure. We define a 1D background velocity model for each station based on the P-velocity model of Perry et al. (2002). The P-wave velocities for each station are then converted to S velocities using a constant V_P/V_S ratio of 1.73. Both S_V and S_H components of receiver function are migrated to depth (to a maximum of 50 km) by the P to S travel time equation (Gurrola et al., 1994; Dueker and Sheehan, 1997),

$$\Delta\, T_{PS}\,(p,z) = \int_z^0 \left(\left\lfloor \left(\frac{R}{V_P\,(z')}\right)^2 - p^2 \right\rfloor^{\frac{1}{2}} - \left\lfloor \left(\frac{1}{V_P\,(z')}\right)^2 - p^2 \right\rfloor^{\frac{1}{2}} \right) dz'.$$

Table 2-1: One dimensional velocity model for all the stations used in this study, extracted from Perry et al. (2002).

A02		**B01**		**B09**	
Depth (km)	**Velocity (km/s)**	**Depth (km)**	**Velocity (km/s)**	**Depth (km)**	**Velocity (km/s)**
1	6	1	6	1	5.8
17.4	6.4	17.4	6.4	19.8	6.4
29.6	6.8	29.6	6.8	28	6.8
35.8	7.2	35.8	7.2	34.2	7.2
50	7.9	50	7.9	50	7.8
A03		**B02**		**B11**	
Depth (km)	**Velocity (km/s)**	**Depth (km)**	**Velocity (km/s)**	**Depth (km)**	**Velocity (km/s)**
1	6	1	6	1	5.8
17.4	6.4	17.4	6.4	27.1	6.4
29.6	6.8	29.6	6.8	34.3	6.8
35.8	7.2	35.8	7.2	35.1	7.2
50	7.9	50	7.9	50	7.8
A04		**B03**		**B12**	
Depth (km)	**Velocity (km/s)**	**Depth (km)**	**Velocity (km/s)**	**Depth (km)**	**Velocity (km/s)**
1	6	1	6	1	6.1
17.4	6.4	17.4	6.4	17.4	6.4
29.6	6.8	29.6	6.8	24.9	6.8
35.8	7.2	35.8	7.2	32.3	7.2
50	7.9	50	7.9	50	7.9
A06		**B04**		**B13**	
Depth (km)	**Velocity (km/s)**	**Depth (km)**	**Velocity (km/s)**	**Depth (km)**	**Velocity (km/s)**
1	5.8	1	5.9	1	5.8
22.5	6.4	16	6.4	27.1	6.4
29.3	6.8	25.9	6.8	34.3	6.8
31.1	7.2	35.7	7.2	35.1	7.2
50	8.2	50	8	50	8

Table 2-1: One dimensional velocity model for all the stations used in this study, extracted from Perry et al. (2002) (continued from previous page).

A07		**B05**		**B15**	
Depth (km)	**Velocity (km/s)**	**Depth (km)**	**Velocity (km/s)**	**Depth (km)**	**Velocity (km/s)**
1	5.8	1	5.9	1	5.8
22.5	6.4	16	6.4	27.1	6.4
29.3	6.8	25.9	6.8	34.3	6.8
31.1	7.2	35.7	7.2	35.1	7.2
50	8.2	50	8	50	8

A08		**B06**	
Depth (km)	**Velocity (km/s)**	**Depth (km)**	**Velocity (km/s)**
1	5.8	1	5.9
22.5	6.4	16	6.4
29.3	6.8	25.9	6.8
31.1	7.2	35.7	7.2
50	8.2	50	8

A09		**B08**	
Depth (km)	**Velocity (km/s)**	**Depth (km)**	**Velocity (km/s)**
1	5.8	1	5.8
22.5	6.4	19.8	6.4
29.3	6.8	28	6.8
31.1	7.2	34.2	7.2
50	8.2	50	7.8

2.4.5 Harmonic decomposition

For an isotropic, horizontally layered medium, all of the energy of the converted S wave will be projected onto the S_V component. Therefore the presence of considerable amount of energy on the S_H component is an indication of dipping and/or anisotropic structure (Cassidy, 1992;

Levin and Park, 1997; Savage, 1998; Frederiksen and Bostock, 2000). The evidence of anisotropy or dipping reflectors in the crustal structure is further manifested in back-azimuthal variations of the amplitude of both S_V and S_H component receiver functions. In cases with a dipping interface or an anisotropic layer in which the symmetry axis is dipping, Ps amplitude and polarity dependence with back-azimuth exhibits a two-lobed (i.e., one cycle) pattern. On the other hand, the pattern becomes four-lobed (two cycles) if an anisotropic layer with horizontal symmetry axis lies beneath the seismometer (e.g., Levin and Park, 1997; Frederiksen and Bostock, 2000; Shiomi and Park, 2008). Both interface dip and anisotropy at the interface cause the S_V and S_H receiver functions to vary with a π/2 phase shift in back-azimuth (Maupin and Park, 2007), as shown in Figure 2-6.

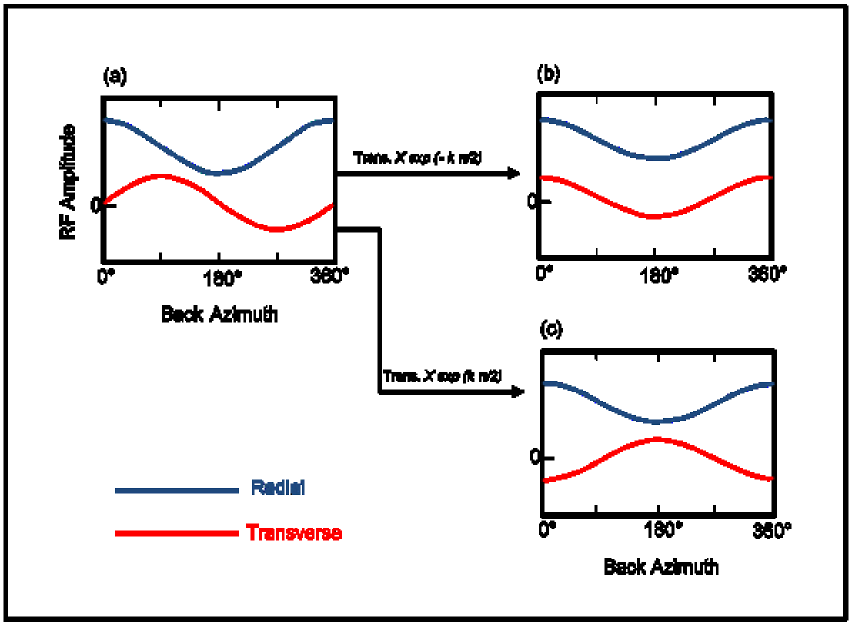

Figure 2-6: Schematic image of radial and transverse component receiver function stacking. (a) Azimuth dependency of receiver functions' amplitude (b,c) comparison of azimuth dependency between radial component and shifted transverse component receiver functions amplitude.

To provide a semi-quantitative interpretation of receiver functions in terms of anisotropy and/or dipping structure, we use a method that decomposes the back-azimuthal variations of depth migrated receiver functions into azimuthal harmonics. This technique, based on stacking receiver functions at various phase shifts in back-azimuths, can be used to map out the orientation of anisotropy that may be related to cracks and/or rock texture caused by deformation.

Decomposing the azimuthal variations of depth migrated receiver functions is based on the extraction of the back-azimuth harmonics of a receiver function data set as a function of the incoming P wave direction. The method assumes that at every depth interval the S_V and S_H amplitudes can be represented as a sum of cos $(k\phi)$ and sin $(k\phi)$, where k is the harmonic degree or order, and ϕ is the back-azimuth (Bianchi et al., 2010). We limit our analysis to the first three degrees and orders, i.e., $k = 0, 1, 2$ (Shiomi and Park, 2008; Bianchi, 2010; Agostinetti et al., 2011; Audet, 2015), therefore producing 5 independent harmonic terms (1, $\cos(\phi)$, $\sin(\phi)$, $\cos(2\phi)$, $\sin(2\phi)$). Degree or order $k = 0$ represents the bulk isotropic variation of the seismic velocities with depth. For flat interfaces in isotropic media, the S_H receiver function contribution disappears and the signals are expressed only on the $k = 0$ back-azimuth harmonic of the S_V receiver function data set, obtained with a simple stack of the S_V receiver function components over back-azimuth. The first and second harmonics, $k = 1, 2$ contain the energy that displays a periodicity of $2\pi/k$ with the back-azimuth ϕ of the incoming P wave. Signal on the $k=1$ component is expected if a dipping interface or an anisotropic layer with a plunging symmetry axis is present at depth, while signal on the $k=2$ component is observed when the subsurface structure includes an anisotropic layer with horizontal symmetry axis (Maupin and Park, 2007; Bianchi, 2010).

The harmonic components are computed by numerically inverting the linear equation relating the set of 2N receiver function amplitude at each depth interval (S_V and S_H components from N events) to the 5 harmonics. Stacking of the S_V and S_H RFs with π /2 shift in back-azimuth enhances the back-azimuth dependency of the P_S pulses. The equation to compute the linear regression of the S_V and S_H components of receiver functions (Bianchi et al., 2010; Audet, 2015) is:

$$\begin{pmatrix} S_{V1}(z) \\ \vdots \\ S_{VN}(z) \\ S_{H1}(z) \\ \vdots \\ S_{HN}(z) \end{pmatrix} = \begin{pmatrix} 1 & \cos(\emptyset_1 - \alpha) & \sin(\emptyset_1 - \alpha) & \cos(2(\emptyset_1 - \alpha)) & \sin(2(\emptyset_1 - \alpha)) \\ \vdots & & & & \\ 1 & \cos(\emptyset_N - \alpha) & \sin(\emptyset_N - \alpha) & \cos(2(\emptyset_N - \alpha)) & \sin(2(\emptyset_N - \alpha)) \\ 0 & \cos(\emptyset_1 - \alpha + \frac{\pi}{2}) & \sin(\emptyset_1 - \alpha + \frac{\pi}{2}) & \cos(2(\emptyset_1 - \alpha) + \frac{\pi}{4}) & \sin(2(\emptyset_1 - \alpha) + \frac{\pi}{4}) \\ \vdots & & & & \\ 0 & \cos(\emptyset_N - \alpha + \frac{\pi}{2}) & \sin(\emptyset_N - \alpha + \frac{\pi}{2}) & \cos(2(\emptyset_N - \alpha) + \frac{\pi}{4}) & \sin(2(\emptyset_N - \alpha) + \frac{\pi}{4}) \end{pmatrix} \begin{pmatrix} A(z) \\ B\|(z) \\ B\perp(z) \\ C\|(z) \\ C\perp(z) \end{pmatrix}$$

The matrix introduces the term α, which represents the orientation of the harmonic terms in a rotated geographic coordinate system. The matrix is inverted at each depth increment within the specified range using singular value decomposition. The term A corresponds to the constant part of the S_V component with respect to the back-azimuth. Thus, the term A represents the bulk isotropic velocity contrasts with depth. In a medium made up of isotropic layers, the term A would contain all the energy of the signal, which means no energy on transverse component. The terms $B\|$ and $B\perp$ contain information on k=1 harmonics in receiver functions. The energy of these terms depend on α with respect to ϕ_i. For α = 0, the k = 1, 2 terms are naturally oriented in the N-S and E-W directions respectively. Therefore, if ϕ_i- α = 0, then $B\|$ will be maximum and $B\perp$ will be close to zero. The same is true for the terms $C\|$ and $C\perp$, which contain information on k = 2 harmonics. The results of tests run on synthetic data shows that the energy on last two terms ($C_\parallel$ and $C_\perp$) is negligible for simple velocity models with either dipping structure or high order symmetry of elastic anisotropy (Bianchi et al., 2010; Agostinetti et al., 2011; Audet, 2015).

In this study we search for the direction, α_C, for which one of the k = 1 component is minimum. Here we keep the decomposition for which the variance on the second k = 1 term is minimum. In fact, the S_V component is maximum when ϕ_N is at a right angle to the strike of a dipping interface, which corresponds to maximum energy on the third harmonic. The recovered angle α can therefore be interpreted as the strike of a dipping interface or the trend of the fast axis of anisotropy (Audet, 2015). In theory the matrix in the above equation could be inverted at each depth increment. However, in practice we have found that searching for α_C over a larger depth range (0 – 50) km, close to the expected depth for Moho at this area (e.g., Cook et al., 2004; Cook and Erdmer, 2005; Mazzotti et al., 2008), gives more stable results shown in section 2.5.

2.5 Results

2.5.1 Radial and transverse receiver function panels

We compute receiver functions and harmonic decomposition for the 19 stations located in the study area. All results are presented in Appendix A. Example results of receiver function data are shown in Figure 2-7 to 2-10 as two separate sets of panels. The first set of panels shows the radial, or S_V, and transverse, S_H, components in the time domain as a function of back-azimuth. The coherence and amplitude of pulses vary at different arrival times. High amplitudes are signs of large variations in elastic impedance, conversion of P phase to S phase and therefore indicate the presence of a discontinuity in seismic velocity. For horizontally layered and isotropic earth structures, the transverse component receiver function is theoretically zero. Periodic phase shifts at a certain arrival times therefore indicate the effect of heterogeneity in subsurface interfaces such as anisotropy and dipping structures. The second set of panels shows the radial and transverse component in the time domain for different values of slowness (or incidence angle). For horizontally layered medium, the arrival time of positive pulses should increase with increasing slowness.

In Figure 2-7 receiver function results for station A02, located in the middle of the study area, are shown. There are three sharp conversion phases at early arrival time of the S_V receiver function component. The first positive pulse (red) at around 1 second, which is continuous for both all back-azimuths and the slowness range, can be a result of very low velocity layer close to the surface. While the arrival time for this first discontinuity is ~0.5 between 120 - 200˚ back-azimuth, it increases to ~1 second for back-azimuths of 230 - 360˚. Immediately after this signal, a negative pulse is found, followed by another high positive amplitude signal at around 3 to 4 seconds. The timing of this last arrival may coincide with the Moho discontinuity at this station. Another negative pulse just below the expected Moho arrival is mostly present between 180 – 360˚ back-azimuths and can be interpreted as a low velocity layer immediately beneath the Moho. Another high-amplitude negative pulse at ~8 seconds may represent mantle layering, or the lithosphere-asthenosphere boundary (LAB). The presence of coherent signals in S_H component receiver functions with several polarity reversals at 150˚ back-azimuth can be an indication of structural heterogeneity and/or anisotropy.

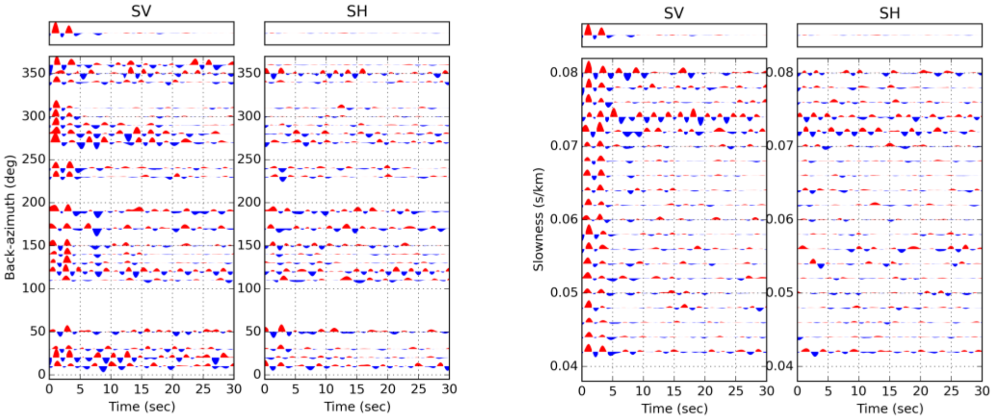

(a)

(b)

Figure 2-7: S_V and S_H receiver function components at station A02 sorted by back-azimuth (a) or slowness (b) as a function of time. The back-azimuth panels show the variations in signal amplitude and polarity that reflect seismic anisotropy. The slowness panels show the moveout (i.e., variation in arrival time as a function of distance from source). The top traces show the average over all back-azimuths and slownesses.

Figure 2-8 shows the receiver function for station A04. The radial component at this station shows some variations in arrival times. For example, the first positive pulse is arriving sooner for back-azimuth between 120˚ - 180˚ in comparison with back-azimuth between 230˚ - 360˚. For some back-azimuth such as 160 - 180˚, there is almost no negative signal at 0 - 3 seconds. The two positive arrivals are followed by a negative pulse at ~4 - 5 seconds. This signature corresponds to the Ps, Pps and Pss arrivals expected from an extremely thin layer of low velocity near the surface. Another important point that is obvious in the receiver function results for this station is the absence of a Moho signal in these data. There is some evidence of polarity reversals at ~5 seconds for 280˚ and 290˚ back-azimuth that can be an indication of structural heterogeneity and/or elastic anisotropy within the crust. However, the transverse component panel for the station A04 contains almost no coherent energy.

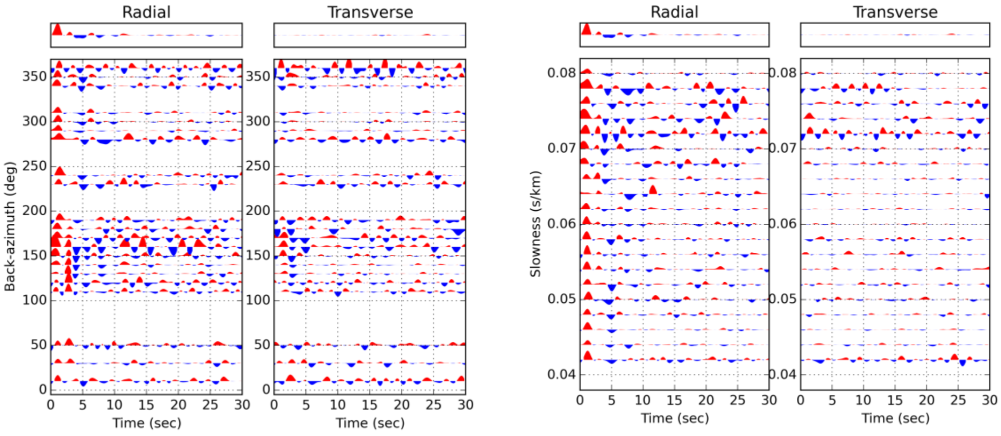

(a) (b)

Figure 2-8: The amplitude variations of radial and transverse receiver function components over (a) back-azimuth, (b) slowness beneath seismic station A04.

Figure 2-9 shows the receiver function results for station B01. This station is located in the middle of the study area close to the station A02. The amplitude variations for the first positive pulse are obvious in the radial panel. The signals between 110˚ and 190˚ back-azimuth are much stronger than those between 230˚ and 360˚. The positive pulse at ~2 seconds is followed by a strong negative response at ~3.5 seconds. Later signals are weaker and show almost no evidence for a strong discontinuity such as the Moho.

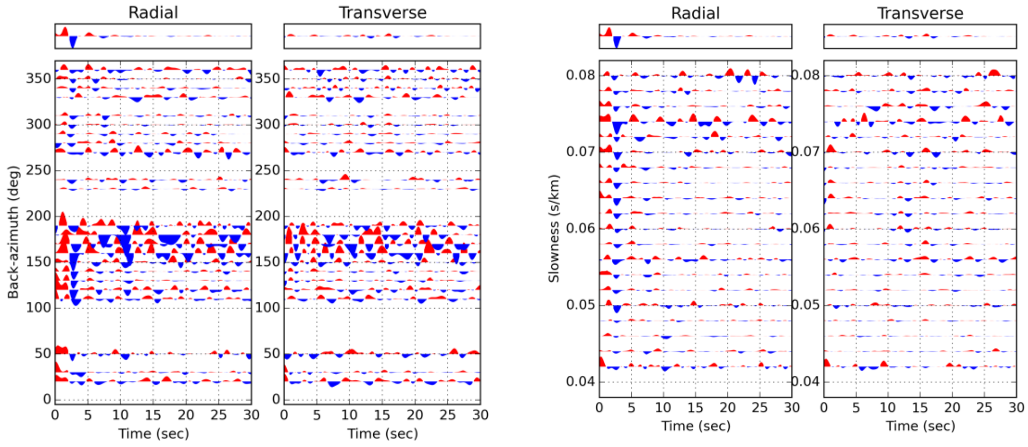

(a) (b)

Figure 2-9: The amplitude variations of radial and transverse receiver function components over (a) back-azimuth, (b) slowness beneath seismic station B01.

Figure 2-10 shows the receiver function panels for the station B15, which is the last station at the western end of the study area within the Cordillera. The back-azimuth coverage between 0 and 100˚ is poor for this station. A low amplitude positive arrival at 0.5 seconds can be seen at 270˚ and 360˚ back-azimuths. Polarity reversal for the first 5 seconds between 100˚ and 140˚ with presence of significant energy in transverse panel can be the result of structural heterogeneity and/or elastic anisotropy. The Moho is evident at ~4 s as a strong positive pulse.

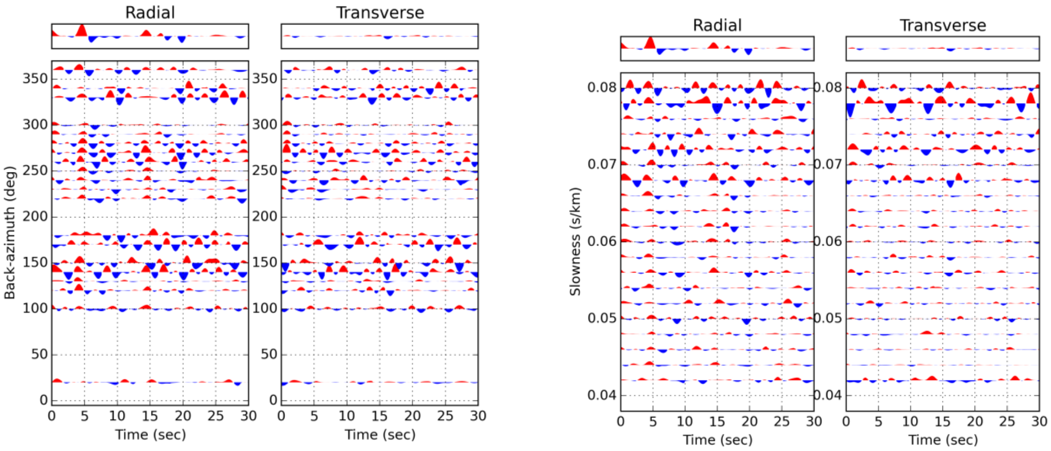

(a) (b)

Figure 2-10: The amplitude variations of radial and transverse receiver function components over (a) back-azimuth, (b) slowness beneath seismic station B15.

2.5.2 Harmonic components

The 5 harmonic components for the same 4 stations are shown in Figures 2-11 to 2-14. The first component A shows the same information as the average of radial receiver functions over all back-azimuths and slowness values (see Figures 2-7 to 2-10). The second and third components correspond to the $\mathrm{B}_{|}$ and $\mathrm{B}\perp$ terms. The component $\mathrm{B}_{|}$ is minimized during the search for the azimuth α_{c}, and therefore displays the least amount of signal, whereas the term $\mathrm{B}\perp$ shows maximum energy. The $\mathrm{C}_{|}$ and $\mathrm{C}\perp$ terms do not show significant amplitude at all depths, and we ignore them in the remainder of the discussion.

Figure 2-11 shows the resolved harmonic decomposition at the station A02. For this station the particular azimuth α_c, corresponding to minimum variation on second term, is 11° indicating that the fast symmetry axis trending 11° or a slow symmetry axis trending 101°. According to this figure, the second term has almost no energy, implying that the dominant direction of α_c = 11° is uniform within the entire crust. Significant energy in $B\perp$ suggests the presence of anisotropy or dipping structure at 20 km depth beneath this station. The second positive pulse at depth 40 km, although it does not have high amplitude, shows anisotropy at this depth. The last two terms have almost no amplitude, as expected for simple structures.

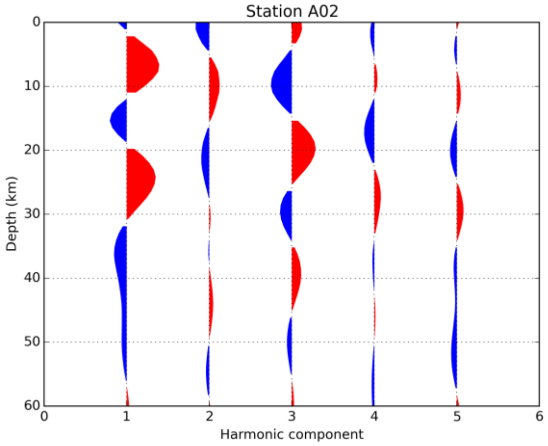

Figure 2-11: Harmonic decomposition components for the station A02. The first component represents term A, the second and third components represent the $B\parallel$ and $B\perp$ respectively. The fourth and fifth components represent the $C\parallel$ and $C\perp$ respectively.

Another example of harmonic decomposition results is shown in Figure 2-12. The resolved α_c for this station is 358˚, thus the slow symmetry axis tending 88˚. There is no significant energy on the second term; therefore the computed α_c can be considered uniform within the entire crust. The strong positive pulse at 22 km depth is pointing to the presence of anisotropy. Although the second positive pulse at ~40 km depth is not as strong as the first one, it indicates the presence of anisotropy.

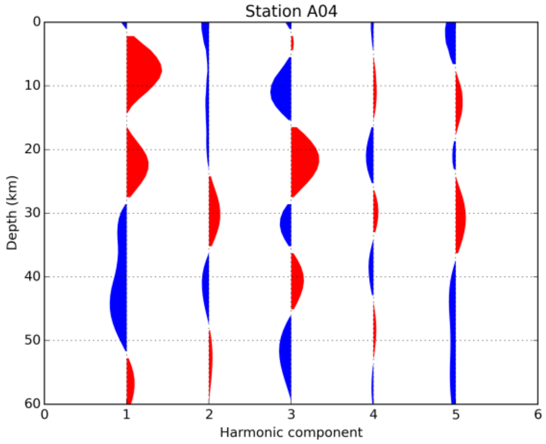

Figure 2-12: Harmonic decomposition components for the station A04.

Figure 2-13 shows the harmonic decomposition for the Station B01. The resolved angle α_c by minimizing the energy on component $B_{\|}$ is 2° for this station. The presence of energy that arises from a discontinuity very close to the surface is observed in the third harmonic component. The second positive pulse at ~15 km is pointing to the presence of anisotropy within the crust beneath this station.

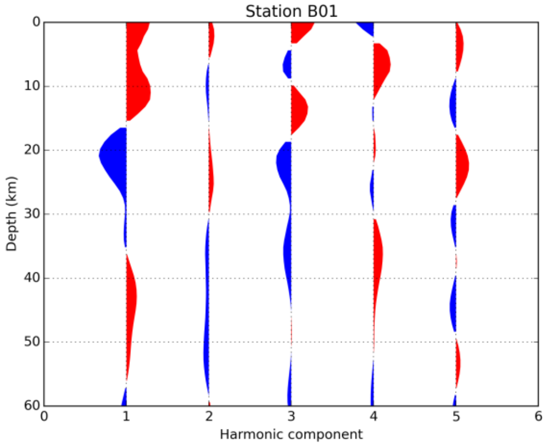

Figure 2-13: Harmonic decomposition components for the station B01.

The harmonic components for station B15 are shown in Figure 2-14. It appears that the harmonic decomposition analysis does not yield meaningful results at this station, probably due to the poor back-azimuth coverage for this station (Figure 2-10). The amount of energy on the second harmonic term does not appear to be minimized. Although the resolved α_c is 133° for this station, we are not able to infer a uniform fast symmetry axis within the entire crust.

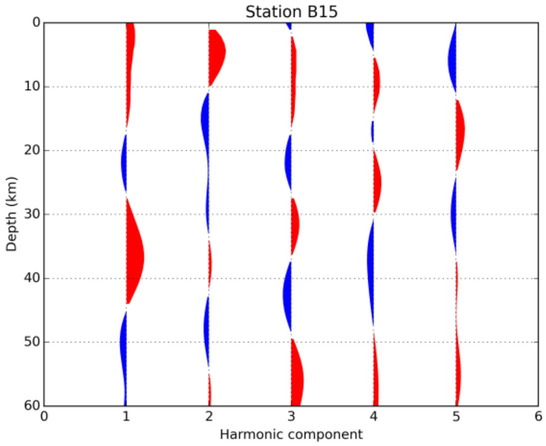

Figure 2-14: Harmonic decomposition components for the station B15.

2.5.3 Profiles of harmonic components

The harmonic components for all seismic stations are projected along two intersecting profiles AA′ and BB′ shown in Figure 2-15. Station A02 is located almost at the intersection point and the other "A" stations, A03-A09, are located towards the northern and eastern part of the study area within a thick sedimentary basin overlying the Canadian Shield. Station B01 is the closest one to the intersection point and the "B" stations, B01-B15, extend toward the western part of the study region.

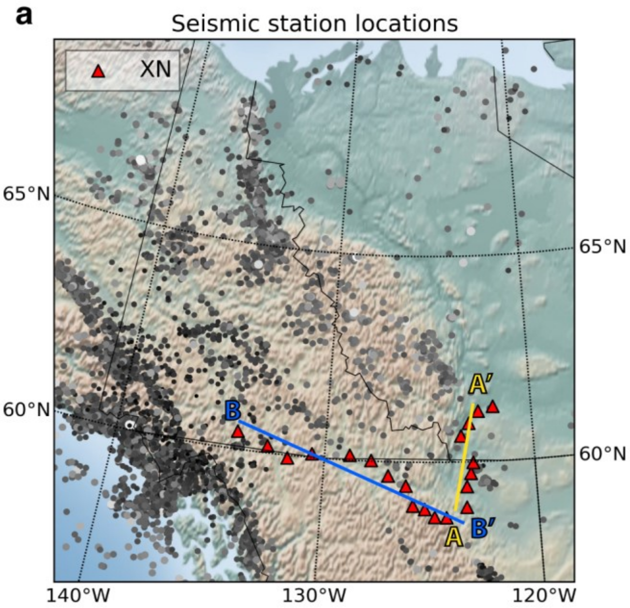

Figure 2-15: Location of seismic stations on the study area along the profiles AA′ and BB′.

The AA′ profile is located entirely within the sedimentary basin. The two panels in Figure 2-16 show the A and B⊥ harmonic terms projected along the AA’ profile. On the A component panel, we observe strong energy between 0 and 30 km depth from alternating positive-negative pulses. Associated with these pulses is strong energy on the B⊥ component. These results are typical of strong reverberations resulting from a thin, low-velocity layer associated with the sedimentary basin. The Ps, Pps and Pss signals are essentially trapped within the layer due to the large contrast across the bottom of the basin and the crystalline basement. The presence of energy on the B⊥ term indicates that the layer is either anisotropic or is dipping, which is consistent with the thickening of the basin toward the west. These signals mask any other structural signal of interest (e.g., the Moho), and we do not interpret these data further.

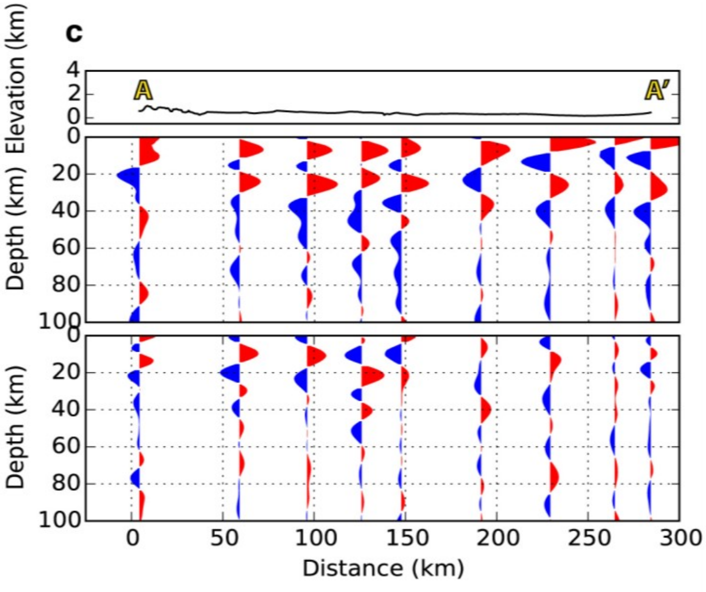

Figure 2-16: A (middle) and B⊥ (bottom) harmonic components projected along the profile AA′. The top panel shows the elevation along the profile.

Figure 2-17 shows the results of the A and B⊥ harmonic terms along profile BB′, which is entirely located within the Cordillera. These results show a clear Moho signal on the A component at around 35-40 km depth, which is consistent with previous studies. The negative pulse located approximately 10 km below the positive pulse of the Moho indicates that the velocity decreases with depth within the mantle below the Moho. The sub-Moho layer therefore represents a high-velocity layer, labelled HVL. Finally, there is an additional negative pulse that seems to be coherent at depth around 70-80 km. This can be an indication of lithosphere-asthenosphere boundary (LAB) produced by a small decrease in seismic velocity across it. The depth of the LAB is slightly higher than other model predictions (e. g., Cook et al., 2004; Cook and Erdmer, 2005; Mazzotti et al., 2008). The signal on the B⊥ component shows high amplitude signal at shallow depth, with a maximum at a depth < 20 km. This suggests a relatively shallow source of anisotropy that varies in polarity and strength along the profile. An additional set of deeper arrivals toward the eastern end of the profile indicates the presence of a westward dipping layer below the Cordillera lithosphere.

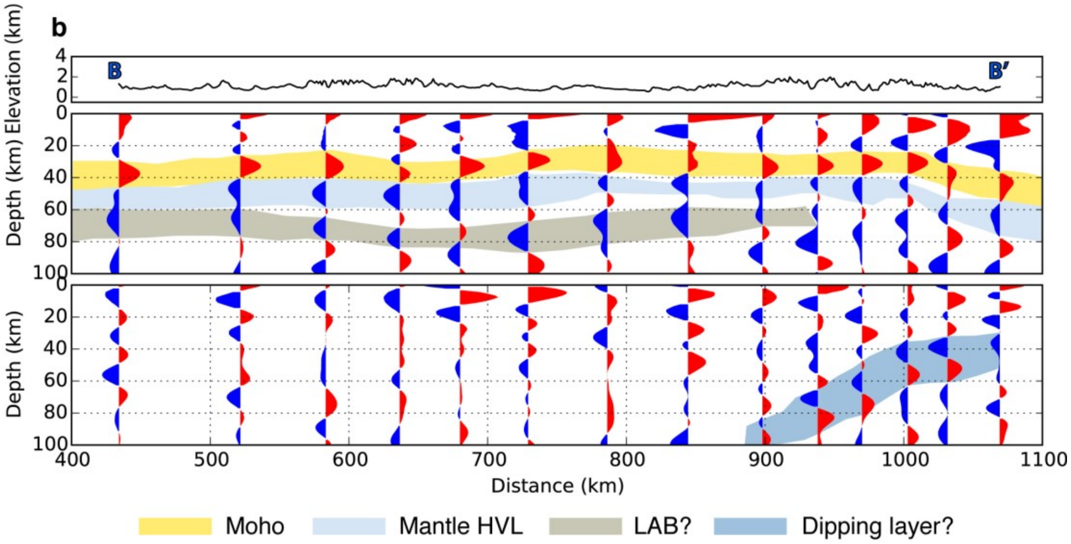

Figure 2-17: A (middle) and B⊥ (bottom) harmonic components projected along the profile BB′. The top panel shows the elevation along the profile.

2.5.4 Variations of anisotropy across the Cordillera

Figure 2-18 shows the azimuths for all the stations computed by minimizing the variance on the second harmonic term. This orientation α_c can be a representation of either the strike of a dipping interface or the orientation of the fast axis of symmetry of anisotropy (or perpendicular to the slow axis of symmetry). There is no coherent orientation over the Cordillera along the BB′ profile, and the anisotropy is seen to rotate from a north-south orientation in the east to more northwest-southeast orientation in the west. On the other hand, on the foreland basin side along the AA′ profile, these azimuths coincide with the strike of the eastward dipping basement, consistent with the thickening of the sedimentary basin. These results are presented in Table 2-2.

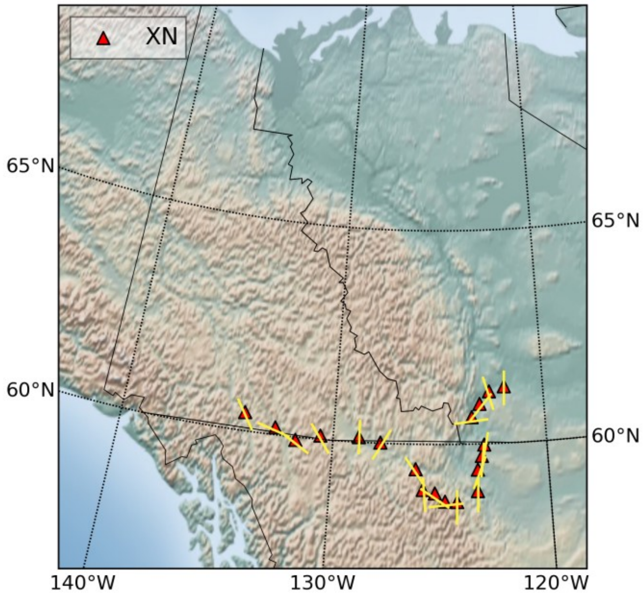

Figure 2-18: Computed azimuths from harmonic decompositios for all stations in the study area.

Table 2-2: Results of fast and slow symmetry axes of anisotropy.

Stations	Latitude	Longitude	Azimuth (deg.)	Slow axis (deg.)
A02	59.4	236.74	11	101
A03	59.72	236.94	176	266
A04	59.98	237.08	358	448
A06	60.63	236.51	248	338
A07	60.94	236.91	232	322
A08	61.22	237.39	167	257
A09	61.33	238.12	186	276
B01	58.9	236.73	2	92
B02	58.65	235.77	176	266
B03	58.66	235.23	152	242
B04	58.85	234.77	127	217
B05	58.93	234.23	163	253
B06	59.42	233.89	40	130
B08	60.01	232.22	150	240
B09	60.12	231.2	321	411
B11	60.09	229.39	357	447
B12	59.93	228.26	212	302
B13	60.17	227.25	21	111
B15	60.43	225.75	133	223

2.6 Discussion

2.6.1 Lithospheric thickness and structures

For stations located along AA′ profile our method of receiver function and harmonic decomposition were not successful to detect the main discontinuity, i.e. the Moho, beneath the seismic stations. The AA′ profile is completely located within the sedimentary basin, thus the receiver function signals are dominated by reverberations caused by low velocity sedimentary layers. The stacked radial receiver functions and the first term, A, of harmonic decompositions imply a low velocity layer up to 10 km thick. This sedimentary layer produces a lot of reverberations within the basin, which can completely hide the structural signals. The presence of amplitude variations with back-azimuths in both radial and transverse receiver function panels for these stations can be the result of dipping layers. Therefore we believe that these anisotropic signals are due to fact that the basement is dipping towards the west, and not to elastic anisotropy.

For BB′ profile located on the Cordilleran side, receiver function data clearly show variations in Moho depth. In particular, the first harmonic terms indicate a flat Moho discontinuity at depths varying between 30 and 35 km, which is expected across the Canadian Cordillera from previous studies. These results also show a ~10 km thick high velocity layer within the uppermost part of mantle just below the Moho. This layer may be associated with an eclogitic layer due to the high temperature and low pressure conditions, although this interpretation is not unique. The lithosphere asthenosphere boundary, LAB, is detectable at a depth of 65 to 80 km according to both the migrated stacked radial receiver function results and the A terms of harmonic decompositions, indicating a thin lithospheric mantle beneath the

Cordillera, which is also consistent with the high heat flow and low elastic thickness values in this region. These results are consistent with the orogenic float model based on thermal isostasy, where elevated temperatures in the upper mantle support the high elevations in the Cordillera, as opposed to having a low-density crustal root.

Interestingly, our results also point to a west-dipping interface across the Cordillera-Craton boundary, which suggests that the lithosphere of the Canadian Shield underlies part of the Cordillera. This may indicate that the lithosphere is slowly sinking via delamination, which would provide an explanation for the source of the high upper mantle temperatures and would further imply that the crust is mechanically decoupled and is slowly uplifting in response to the sinking lithospheric mantle layer. Thermo-chronology data may help to constrain this conceptual model.

2.6.2 Origin of anisotropy

According to receiver function data along the AA′ and BB′ profiles within the study area and the harmonic decomposition panels, we are able to detect the presence of crustal heterogeneity across the northern Canadian Cordillera. The existence of high amplitude pulses on the third harmonic terms represent crustal anisotropy at depths varying between 5 and 20 km, which therefore do not extend in the lower crust. However, the presence of this upper crustal anisotropy may be the consequence of regional tectonics such as dipping layers and/or crustal fabrics and the orientation of minerals. Based on the results and the geology of the area, we believe that the presence of anisotropy along the AA′ profile within the sedimentary basin is caused by the westward dipping basement of the sedimentary basin. The slow directions along

BB′ profile are highly variable, and there is no consistent orientation of anisotropy over the Cordillera.

Receiver function and teleseismic shear wave splitting (SKS) data around the Denali Fault in southwest Yukon, which is located in the western part of our BB′ profile, indicate the presence of fossilized transpression fabric in crustal and upper-mantle anisotropy along this fault (Rasendra et al., 2014). These authors interpret the observed present day anisotropy in the middle crust to be the result of highly deformed oriented fabrics, foliated felsic rocks such as gneiss or schists, in deeper mid to lower crust shear zone (Rasendra et al., 2014). The fossilized structural and mineral fabrics are localized around the fault and do not produce a strong coherent signal through a large region (Rasendra et al., 2014), in contrast to our results of anisotropy.

2.7 Summary

In this study we carried out a receiver function analysis and harmonic decomposition to characterize lithospheric structure and anisotropy beneath 19 seismic stations across the northern Canadian Cordillera, using data from 379 teleseismic earthquakes. The seismograms were processed to rotate the 3 components into a frame of reference aligned with the incoming direction of the earthquake waves. In this rotation the vertical direction remains the same, though the two horizontal components are rotated into the radial and transverse components. Then we produced an approximate impulse response of the subsurface beneath the individual seismic station (i.e., receiver functions) by deconvolving the P component from the S_V and S_H components by using a modified Wiener-spectral deconvolution. In order to determine the depth of all velocity and phase changes in both S_V and S_H components of receiver function data, we migrated both these receiver function data sets into the depth domain using a one dimensional background velocity model before running the harmonic decomposition analysis. We observe high amplitude pulses at depths between 30 and 35 km for some stations mostly on the BB′ profile located in the northern Canadian Cordillera that indicate a continuous and flat Moho. Receiver function data for stations located on top of thick sedimentary sequences on the adjacent Canadian Shield did not generate useful signals due to large reverberations within the sedimentary structures that mask deeper structural signals.

Amplitude and phase variations with back-azimuth of receiver function data indicate the effects of anisotropy and/or dipping structures. We process the receiver function data using a harmonic decomposition to characterize the periodic variations and to analyze the anisotropy based on both radial and transverse receiver function results. We find upper crustal anisotropy at shallow depth (between 5 and 20 km) with fast axis orientation varying on short spatial scales. On the foreland basin side we believe that the anisotropy may be the result of east-dipping reflectors associated with the base of the sedimentary basins. The relatively thin layer of anisotropy detected by these seismic data is consistent with the results from active source seismic studies. In addition, this low crustal thickness supports the model of high heat flow due to elevated mantle temperature (i.e., thermal Finally, isostasy) in the northern Canadian Cordillera. The detachment between brittle upper crust and weak ductile lower crust (i.e., the bottom of the anisotropic layer) can provide an explanation for the transmission of stress from the plate boundary to the west, resulting in the seismic and tectonic activities far from the plate boundaries.

Finally, there appears to be a ~10 km thick high velocity lid in the upper most mantle across the Cordillera. This lid might be associated with eclogitized material. The lithosphere asthenosphere boundary is detectable by negative pulses at depth between 65 and 80 km, implying that the lithospheric mantle is ~30-50 km thick beneath the Cordillera. These results are consistent with the orogenic float model of Mazzotti and Hyndman (2002).

3. CONCLUSION

Knowledge of crustal structure in active orogens is important in constraining tectonic models characterized by rapid deformation in order to understand processes associated with mountain building. In this study we extracted information on the structure of the crust and mantle across the northern Canadian Cordillera using teleseismic data. In particular, we inferred the depth of Moho and the lithospheric thickness, in addition to characterizing the structural heterogeneity and seismic anisotropy in this region.

We selected the receiver function analysis technique and applied it to 19 seismic stations located within the study area. Our results show that the presence of low velocity layers, such as those in foreland sedimentary basins, completely mask the pulses from a deeper discontinuity such as the Moho. Producing lots of reverberation within the low velocity layer mostly contribute in eradicating the real resolution of receiver function results. However receiver function data were successful to resolve the subsurface structure beneath the stations on the Cordilleran side. The average depth of Moho is ~32 km.

When good coverage of back-azimuth and high signal to noise ratio are available for teleseismic data, the harmonic decomposition technique can be used to visualize the presence of anisotropy within the crust. We detected upper crustal anisotropy across the study area and provided the orientation of either the strike of a dipping interface or the orientation of the fast axis of symmetry of anisotropy. Although receiver function data are unable to detect discontinuities in presence of very low velocity layers such as sedimentary basin structures, it might be possible to use a processing method applicable for this setting in order to reduce the effect of very low velocity layers. Alternatively, it would be advantageous to try another seismic analysis technique (e.g., surface-wave tomography) to find the Moho depth in our study area.

The presence of a high velocity layer in the mantle cannot be explained by the orogenic flout model, as it predicts a homogeneous mantle due to the vigorous convection. We think that this high velocity layer contains eclogite. When mafic rocks are in high pressure and high temperature conditions they get more compact (denser) and form eclogite. The validity of this idea can be examined for example by extracting the seismic velocities at that specific depth and then compare them with the laboratory velocities for this kind of rock.

Constraining the origin of anisotropy is another area where further work is warranted. Detail geological setting information such as type of the rocks and their physical properties can be useful input data to build a more precise velocity model as well as producing more accurate outputs regarding quantitative anisotropy. To this end, we suggest using synthetic data in a formal inversion procedure to help construct the best velocity model and measuring the amount of anisotropy.

REFERENCES

Agostinetti, N. P., Park, J., and Lucente F. P., 2008b. Mantle wedge anisotropy in Southern Tyrrhenian subduction zone (Italy), from receiver function analysis, Tectonophysics, 462, 35-48, doi:10.1016/j.tecto.2008.03.020.

Agostinetti, N. P., Steckler, M., and Lucente, F. P., 2009. Imaging the subducted slab under the Calabrian Arc, Italy, from receiver function analysis, Lithosphere,1(3), 131–138, doi:10.1130/L49.1.

Agostinetti, N. P., Bianchi, I., Amato, A., and Chiarabba, C., 2011. Fluid migration in continental subduction: The Northern Apennines case study, Earth and Planetary Science Letters, 302, 267–278,636.

Ammon, C. J., 1991. The isolation of receiver effects from teleseismic P waveforms, Bulletin of the Seismological Society of America, 81, 2504–2510.

Ammon, C. J., and Zandt, G., 1993. Receiver structure beneath the southern Mojava block, California, Bulletin of the Seismological Society of America, 83, 737-755.

Anderson, D. L., 1989. Theory of the Earth Chapter 15. Anisotropy, Boston: Blackwell Scientific Publications, http://resolver.caltech.edu/CaltechBOOK:1989.001.

Audet, P., Jellinek, A. M., Uno, H., 2007. Mechanical controls on the deformation of continents at convergent margins, Earth and Planetary Science, 264, 151–166.

Audet, P., 2010. Temporal variations in crustal scattering structure near Parkfield, California, using receiver functions, Bulletin of the Seismological Society of America, 100, 1356–1362.

Audet, P., 2015. Layered crustal anisotropy around the San Andreas Fault near Parkfield, California, Journal of Geophysical Research, doi:10.1002/2014JB011821, in press.

Bannister, S., Reyners, M., Stuart, G., and Savage, M., 2007. Imaging the Hikurangi subduction zone, New Zealand, using teleseismic receiver functions: Crustal fluids above the forearc mantle wedge, Geophysical Journal International, 169, 602–616.

Bianchi, I., 2010. Velocity structure and seismic anisotropy in the crust and upper-mantle from Receiver Function analysis: three case studies in Italy, PhD thesis, Alma Mater Studiorum – Universita' di Bologna, Bologna, Italy.

Bianchi, I., Park, J., Agostinetti, N. P., and Levin, V., 2010. Mapping seismic anisotropy using harmonic decomposition of receiver functions: An application to Northern Apennines, Italy, Journal of Geophysical Research, 115, B12317, doi:10.1029/2009JB007061.

Bostock, M. G., 1998. Mantle stratigraphy and evolution of the Slave province, Journal of Geophysical Research, 103, 21,183–21,200.

Bourne, M., and Stuart, G., 2000. ScSp observed on North Island, New Zealand: implications for subducting plate structure, Geophysical Journal International, 142, 925-932.

Burdick, L. J., and Langston, C. A., 1977. Modeling crustal structure through the use of converted phases in teleseismic body-waveforms, Bulletin of the Seismological Society of America, 67, 677-691.

Cassidy, J. F., and Ellis, R. M., 1991. Shear wave constraints on a deep crustal reflective zone beneath Vancouver Island, Journal of Geophysical Research, 96, 19,843–19,851.

Cassidy, J. F., 1992. Numerical experiments in broadband receiver function analyses, Bulletin of the Seismological Society of America, 82, 1453–1474.

Clowes, R. M., Zelt, C. A., Amor, J. R., and Ellis, R. M., 1995. Lithospheric structure in the southern Canadian Cordillera from a network of seismic refraction lines, Canadian Journal of Earth Sciences, 32, 1485–1513.

Clowes, R. M., Calvert, A. J., Eaton, D. W., Hajnal, Z., Hall, J., and Ross, G. M., 1996. Lithoprobe reflection studies of Archean and Proterozoic crust in Canada, Tectonophysics, 264, 65–88.

Clowes, R. M., and Hammer, P. T. C., 2000. Comparison of Lithospheric Structures Across the Alaskan and Canadian Cordillera , GeoCanada, Technical Session 18, Abstract#529 (on CD).

Colpron, M., 2006. Tectonic assemblage map of Yukon-Tanana and related terranes in Yukon and northern British Columbia, Yukon Geological Survey, Open File 2006-1, scale 1:1,000,000.

Colpron, M., Nelson, J. L., and Murphy, D. C., 2007. Northern Cordilleran terranes and their interactions through time, GSA Today, 17, no. 4/5, doi: 10.1130/GSAT01704-5A.1.

Cook, F. A., Clowes, R. M., Snyder, D. B., van der Velden, A. J., Hall, K. W., Erdmer, P., and Evenchick, C. A., 2004. Precambrian crust beneath the Mesozoic northern Canadian

Cordillera discovered by Lithoprobe seismic reflection profiling, Tectonics, 23, TC2010, doi:10.1029/2002TC001412.

Cook, F. A., and Erdmer, P., 2005. An 1800 km cross section of the lithosphere through the northwestern North American plate: lessons from 4.0 billion years of Earth's history, Canadian Journal of Earth Sciences, 42, 1295–1311.

Dey-Sarker, S. K., and Wiggins, R. A., 1976. Upper mantle structure in western Canada. Journal of Geophysical Research, 81, 3619-3632.

Dueker, K. G., and Sheehan, A. F., 1997. Mantle discontinuity structure from midpoint stacks of converted P and S waves across the Yellow-stone hotspot track, Journal of Geophysical Ressearch, 102, 8313-8327.

Farra, V., and Vinnik, L., 2000. Upper mantle stratification by P and S receiver functions, Geophysical Journal International, 141, 699-712.

Ferris, A., Abers, G. A., Christensen, D. H., and Veenstra, E., 2003. High resolution image of the subducted Pacific (?) plate beneath central Alaska, Earth and Planetary Science Letters, 214, 575-588.

Flück, P., Hyndman, R. D., and Lowe, C., 2003. Effective elastic thickness T_e of the lithosphere in western Canada, Journal of Geophysical Research, 108, NO. B9, 2430, doi:10.1029/2002JB002201.

Fouch, M. J., and Rondenay, S., 2006. Seismic anisotropy beneath stable continental interiors, Physics of the Earth and Planetary Interiors, 158, 292320.

Frassetto, A. M., Zandt, G., Gilbert, H., Owens, T. J., and Jones, C. H., 2011. Structure of the Sierra Nevada from receiver functions and implications for lithospheric foundering, Geosphere, 7, 898-921.

Frederiksen, A. W., 2000. Seismic imaging of the Canadian upper mantle, PhD thesis, University of British Columbia.

Frederiksen, A. W., and Bostock, M. G., 2000. Modelling teleseismic waves in dipping anisotropic structures, Geophysical Journal International, 141, 401–412.

Gabrielse, H., 1985. Major dextral transcurrent displacements along the Northern Rocky Mountain Trench and related lineaments in north-central British Columbia, Geological Society of America Bulletin, 96, 1–14.

Gabrielse, H., Monger, J. W. H., Wheeler, J. O., and Yorath, C. J., 1991. Part A. Morphogeological belts, tectonic assemblages, and terranes, in Chapter 2 of Geology of the Cordilleran Orogen in Canada: Geological Survey of Canada, Geology of Canada, 4, 15-28. (also Geological Society of America, The Geology of North America, v. G-2).

Gabrielse, H., and Yorath, C. J., 1989. DNAG #4: The Cordilleran orogen in Canada, Geoscience Canada, 16, 67-83.

Galetti, E., and Curtis, A., 2012. Generalised receiver functions and seismic interferometry, Tectonophysics 532-535, 1-26.

Gurrola, H., Minster, J. B., and Owens, T., 1994. The use of velocity spectrum for stacking receiver functions and imaging upper mantle discontinuities, Geophysical Journal International, 117, 427–440.

Hyndman, R. D., Flück, P., Mazzotti, S., T. J. Lewis, Ristau, J., and Leonard, L., 2005. Current tectonics of the northern Canadian Cordillera, Canadian Journal of Earth Sciences, 42, 1117-1136.

Iidaka, T., and Obara, K., 1993. The upper boundary of the subducting Paci®c Plate estimated from ScSp waves beneath the Kanto region, Journal of Physics of the Earth, 41, 103-108.

Kawakatsu, H., and Watada, S., 2007. Seismic evidence for deep water transportation in the mantle, Science, 306, 1468–1471.

Langston, C. A., 1977. Corvallis, Oregon, crustal and upper mantle structure from teleseismic P and S waves, Bulletin of the Seismological Society of America, 67, 713-724.

Langston, C. A., 1979. Structure under Mount Rainier, Washington, inferred from teleseismic body waves, Journal of Geophysical Research, 84, 4749-4762.

Langston, C. A., 1989. Scattering of teleseismic body waves under Pasadena, California, Journal of Geophysical Research, 94, 1935-1951.

Levin, V., and Park J., 1997. P-SH conversions in a flat-layered medium with anisotropy of arbitrary orientation, Geophysical Journal International, 131, 253–266.

Levin, V., and Park, J., 1998. P-SH conversions in layered media with hexagonally symmetric anisotropy: a cookbook, Pure and applied Geophysics, 151, 669-697.

Lin, C. H., 1995. A Review of Receiver Function Techniques for Estimation of One-Dimensional Velocity Structures, TAO, 6, No.2, 181-195.

Lines, L. R., and Treitel, S., 1984. Tutorial: a review of least-squares inversion and its application to geophysical problems, Geophysical Prospecting, 32, 159-186.

Maupin, V., and Park, J., 2007. Theory and observations: Wave propagation in anisotropic media, Treatise on Geophysics, 1, Seismology and Structure of the Earth, edited by Romanowicz, B., and Dziewonski, A., 289–321, Elsevier, New York.

Mazzotti, S., and Hyndman, R. D., 2002. Yakutat collision and strain transfer across the northern Canadian Cordillera, Geology, 30, 495-498.

Mazzotti, S., Leonard, L. J., Hyndman, R. D., and Cassidy, J. F., 2008. Tectonics, dynamics, and seismic hazard in the Canada–Alaska Cordillera, American Geophysical Union, 179, 297-319.

Monger, J. W. H., Price, R. A., and Tempelman-Kluit, D. J., 1982. Tectonic accretion and the origin of two metamorphic and plutonic welts in the Canadian Cordillera: Geology, 10, 70–75.

Monger, J. W. H., and Price, R. A., 2002. The Canadian Cordillera: Geology and tectonic evolution, CSEG Rec., 17–36, February.

Nabelek, J., Hetenyi, G., Vergne, J., Sapkota, S., Kafle, B., Jiang, M., Chen, J., Huang, B. S., and the Hi-CLIMB team, 2009. Underplating in the Himalaya-Tibet collision zone revealed by the Hi-CLIMB experiment, Science, 325, 1371–1374.

Nakanishi, I., Suyehiro, K., and Yokota, T., 1981. Regional variations of amplitudes of ScSp phases observed in the Japanese Islands, Geophysical Journal of the Royal Astronomical Society, 67, 615-634.

Nikulin, A., Levin, V., and Park, J., 2009. Receiver function study of the Cascadia megathrust: Evidence for localized serpentinization, Geochemistry Geophysics Geosystems, 10, Q07004, doi:10.1029/2009GC002376.

Park, J., Yuan, H., and Levin, V., 2004. Subduction zone anisotropy beneath Corvallis, Oregon: A serpentinite skid mark of trench-parallel terrane migration?, Journal of Geophysical Research, 109, B10306, doi:10.1029/2003JB002718.

Perry, H. K. C., Eaton, D. W. S., and Forte, A. M., 2002. LITH5.0: a revised crustal model for Canada based on Lithoprobe results, Geophysical Journal International, 150, 285–294.

Rasendra, N., Bonnin, M., Mazzotti, S., and Tiberi, C., 2014. Crustal and upper-mantle anisotropy related to fossilized transpression fabric along the Denali fault, northern Canadian Cordillera, Bulletin of the Seismological Society of America, 104, 1964-1975.

Rondenay, S., Bostock, M. G., and Shragge, J., 2001. Multiparameter two-dimensional inversion of scattered teleseismic body-waves Application to the Cascadia 1993 data set, Journal of Geophysical Research, 106, 30795-30807.

Savage, M., 1998. Lower crustal anisotropy or dipping boundaries? Effects on receiver functions and a case of study in New Zealand, Journal of Geophysical Research, 103, 15069-15087.

Shiomi, K., and Park, J., 2008. Structural features of the subducting slab beneath the Kii Peninsula, central Japan: Seismic evidence of slab segmentation, dehydration, and anisotropy, Journal of Geophysical Research, 113, Doi: 10.1029/2007JB005535.

Silberling, N. J., Jones, D. L., Monger, J. W. H., and Coney, P. J., 1992. Lithotectonic terrane map of the North American Cordillera, U.S. Geological Survey Miscellaneous Investigation Map I-2176, scale 1:5,000,000.

Snoke, J., Sacks, S., and Okada, H., 1977. Determination of the subducting lithosphere boundary by use of converted phases, Bulletin of the Seismological Society of America, 67, 1057-1060.

Snyder, D. B., Clowes, R. M., Cook, F. A., Erdmer, P., Evenchick, C. A., van derVelden, A. J., and Hall, K. W., 2002. Proterozoic prism arrests suspect terranes: insights into the ancient Cordilleran margin from seismic reflection data, GSA Today, 12(10), 4–10.

Sodoudi, F., 2005. Lithospheric structure of the Aegean obtained from *P* and *S* receiver functions, PhD thesis, Freie Universität Berlin.

Thompson, R. I., Mercier, E., and Rosts, C. F., 1987. Extension and its influence on Canadian Cordilleran passive margin evolution, Geological Society, London, Special Publications, 28, 409-417, doi: 10.1144/GSL.SP.1987.028.01.25.

Thomsen, L., 2002. Understanding seismic anisotropy in exploration and exploitation. SEG-EAGE Distinguished Instructor Series 5. Society of Exploration Geophysicists.

Thorkelson, D. J., Mortensen, J. K., Creaser, R. A., Davidson, G. J., and Abbott, J. G., 2001. Early Proterozoic magmatism in Yukon, Canada: constraints on the evolution of northwestern Laurentia, Canadian Journal of Earth Sciences, 38, 1479– 1494.

Vinnik, L. P., 1977. Detection of waves converted from P to SV in the mantle, Physics of the Earth and Planetary Interiors, 15, 39–45.

Wheeler, J. O., Brookfield, A. J., Gabrielse, H., Monger, J. W. H., Tipper, H. W., and Woodsworth, G. J. (compilers), 1991. Terrane map of the Canadian Cordillera, Geophysical Survey of Canada, Map 1713A, scale 1:1 000 000, 2 sheets.

Wiener, N., 1964. Extrapolation, Interpolation, and Smoothing of Stationary Time Series, Cambridge, Mass: MIT Press. ISBN 0-262-73005-7.

Zelt, C. A., Ellis, R. M., Zelt, B. C., 2006. Three-dimensional structure across the Tintina strike-slip fault, northern Canadian Cordillera, from seismic refraction and reflection tomography, Geophysical Journal International, 167, 1292-1308.

Zhu, L., and Kanamori, H., 2000. Moho depth variation in southern California from teleseismic receiver functions, Journal of Geophysical Research, 105, 2969-2980.

APPENDIX

Receiver function and harmonic decomposition results for all stations used in this study.

Station A02:

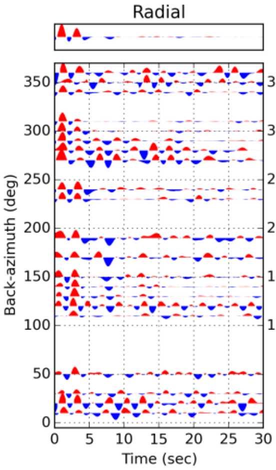

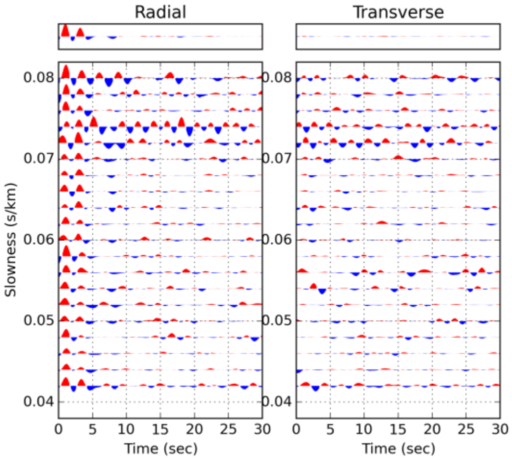

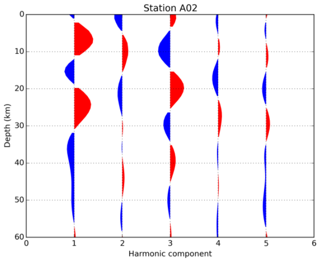

Station A03:

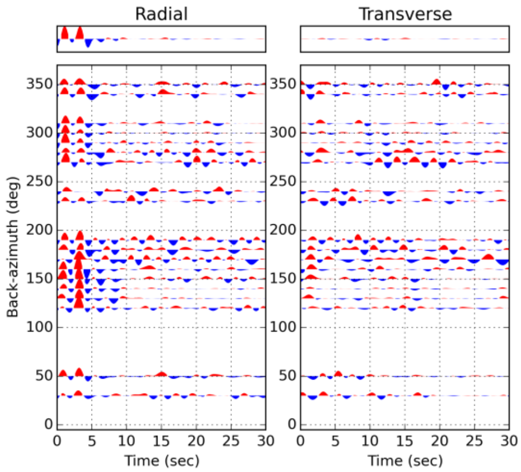

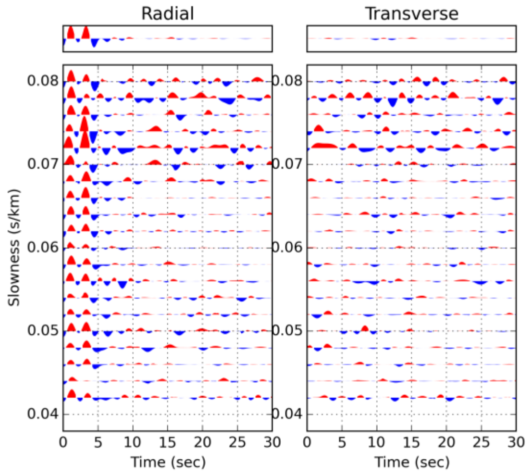

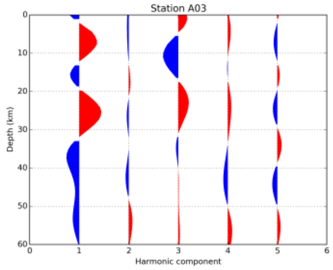

Station A04:

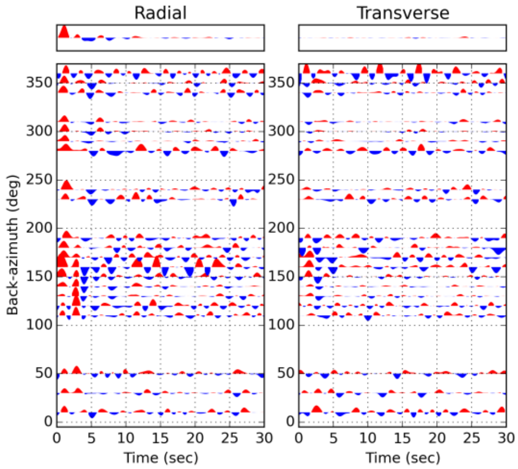

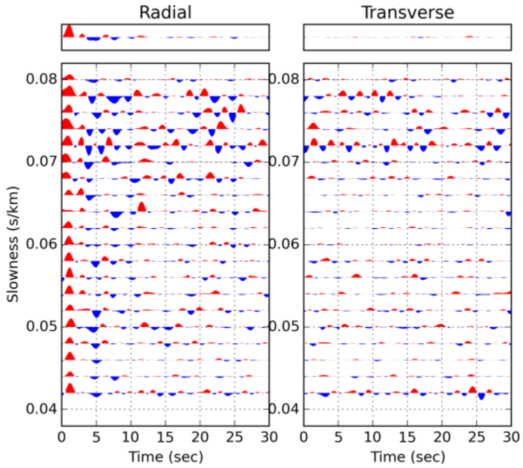

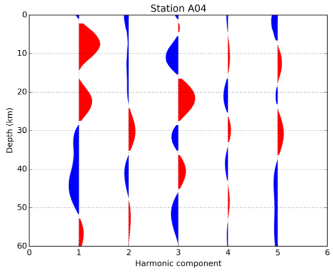

Station A06:

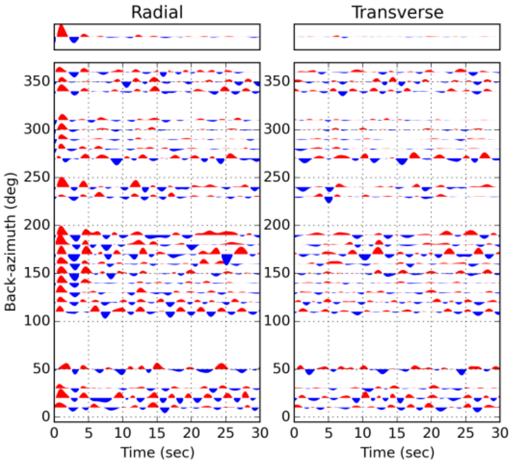

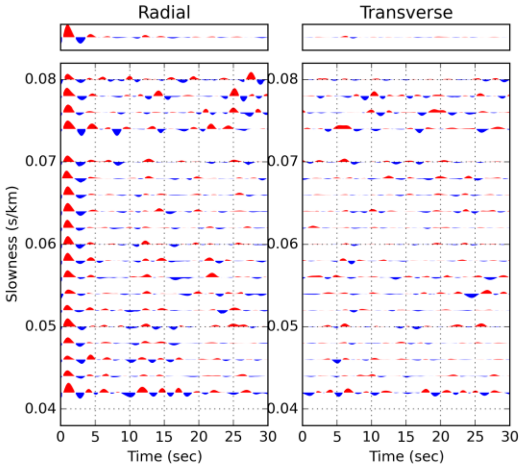

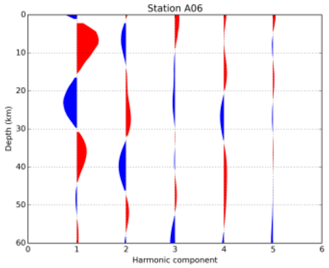

Station A07:

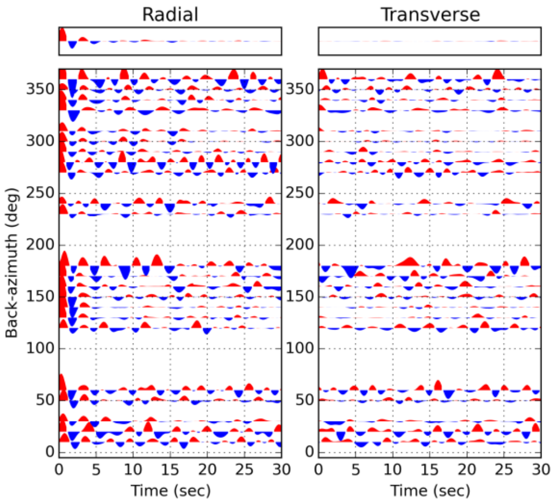

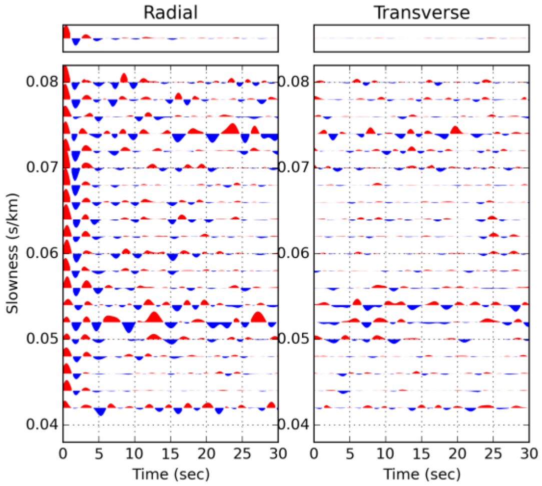

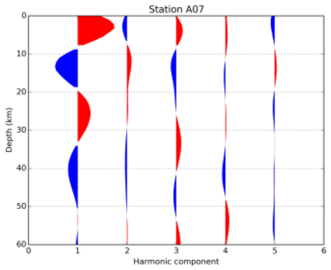

Station A08:

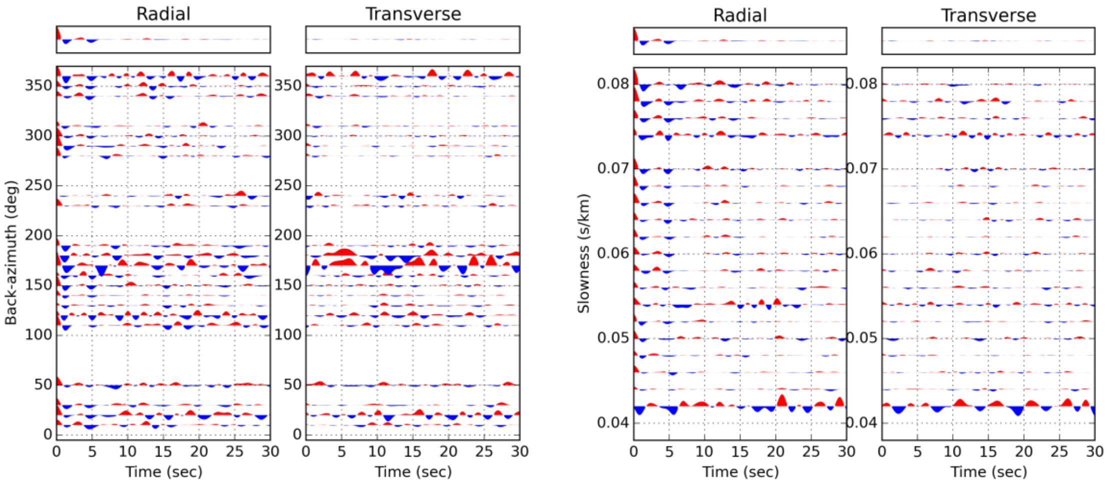

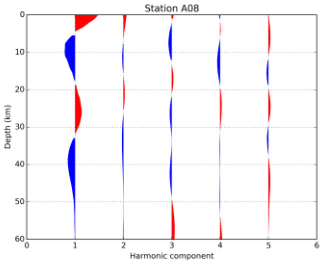

Station A09:

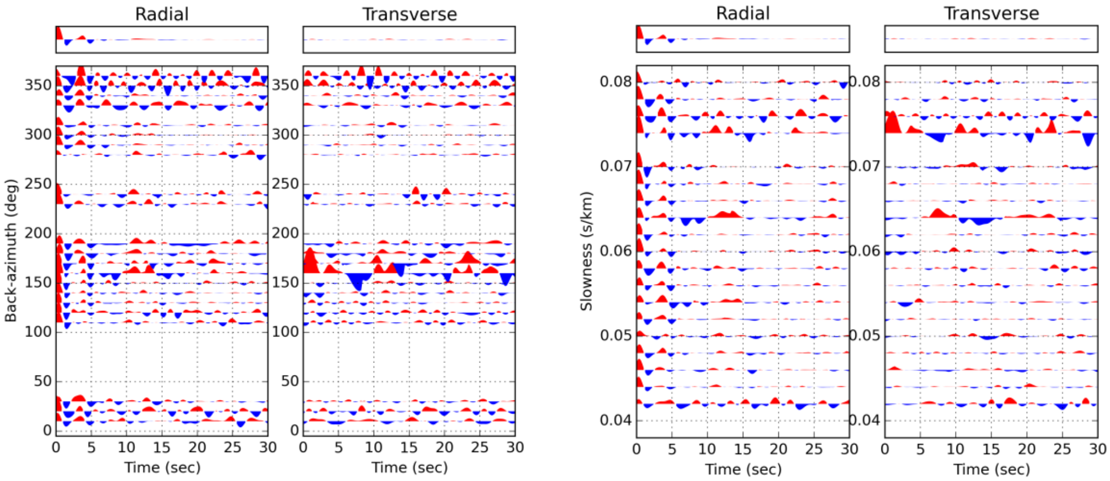

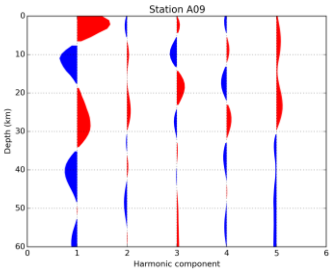

Station B01:

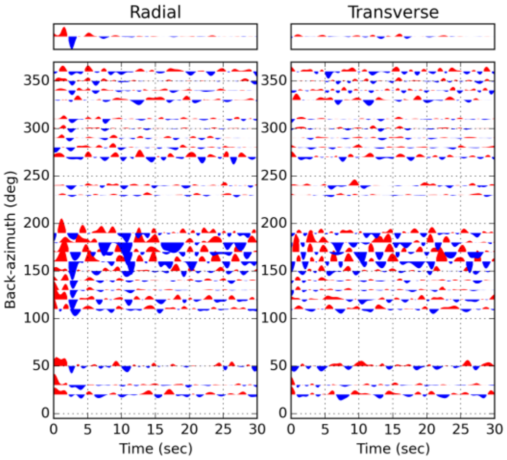

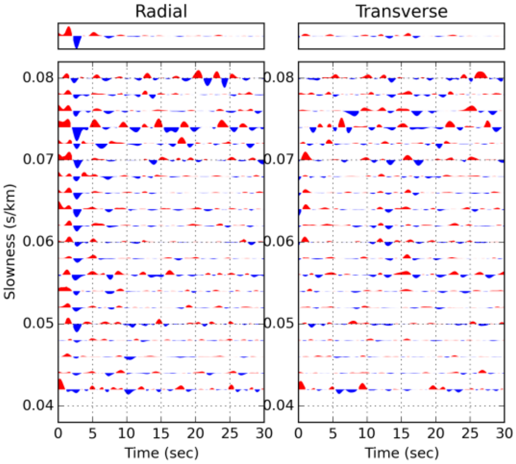

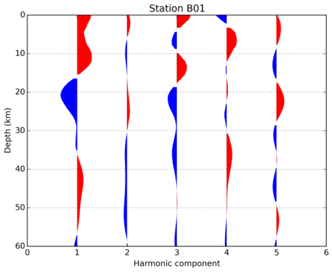

Station B02:

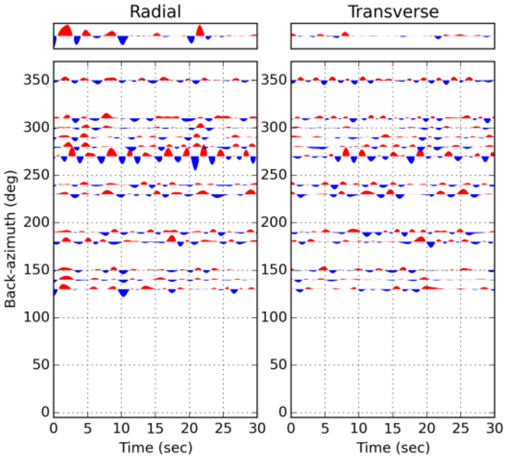

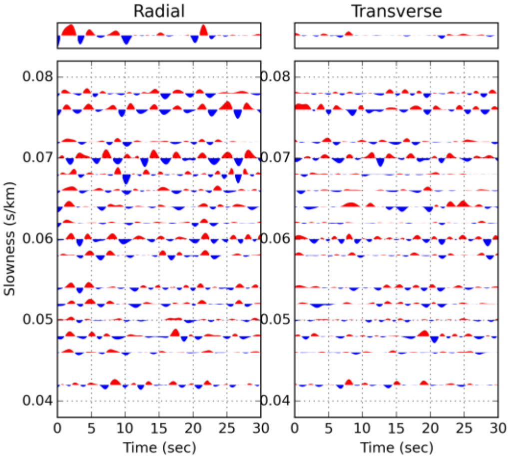

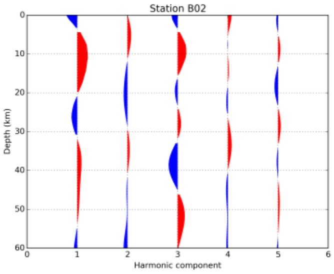

Station B03:

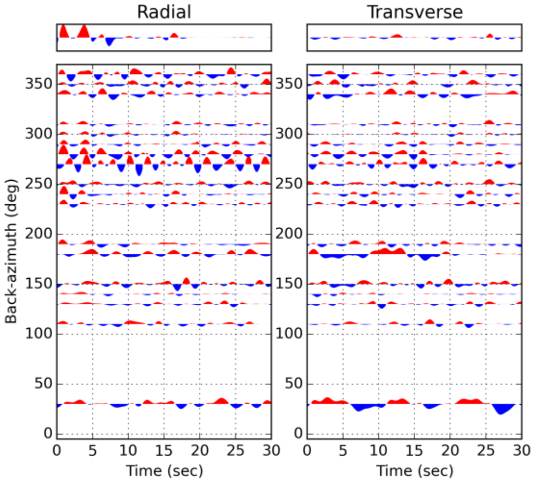

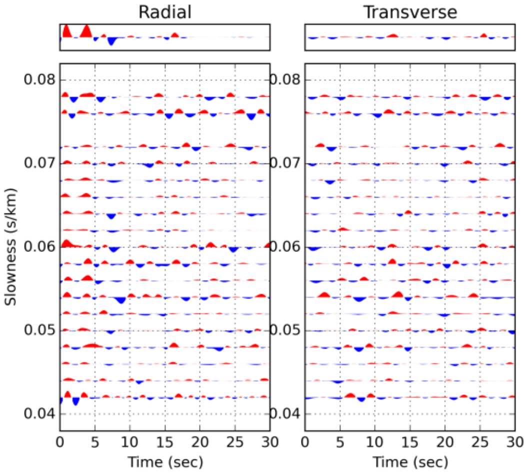

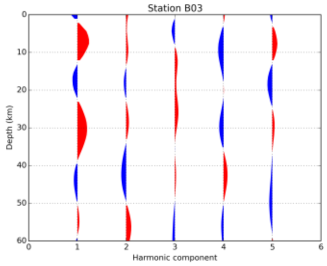

Station B04:

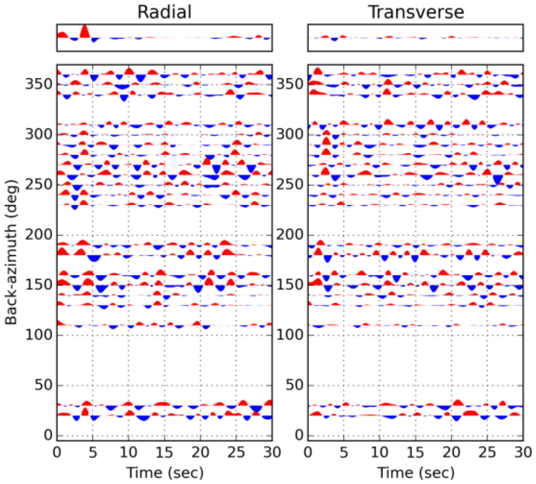

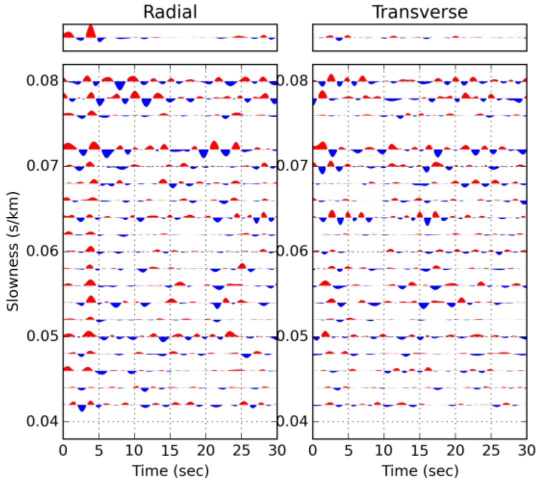

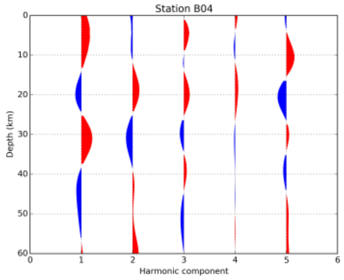

Station B05:

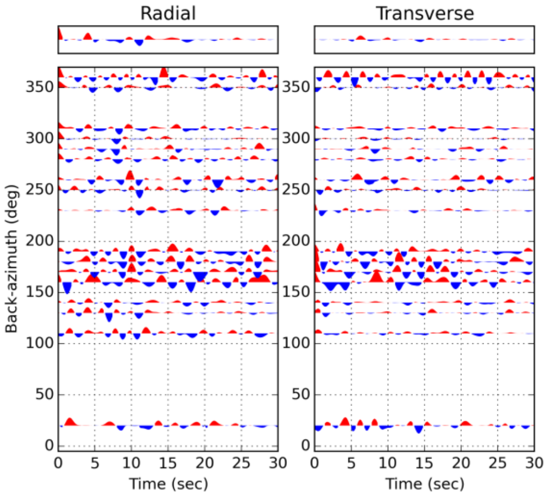

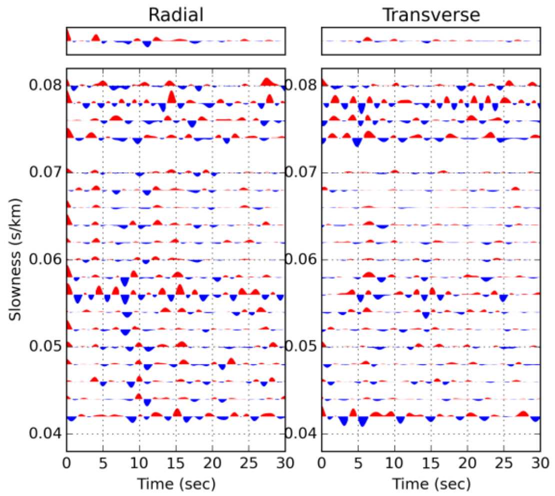

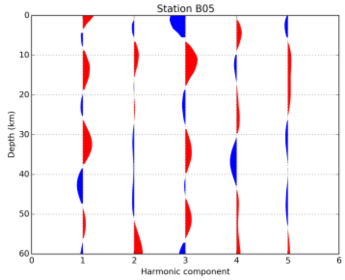

Station B06:

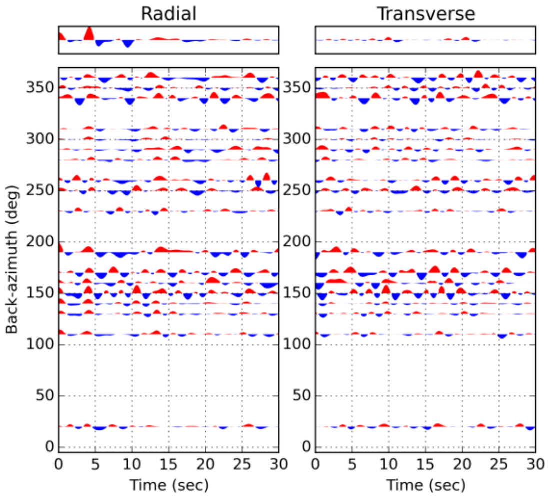

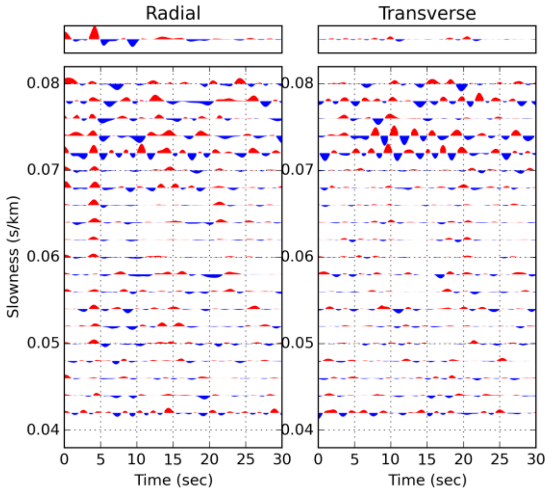

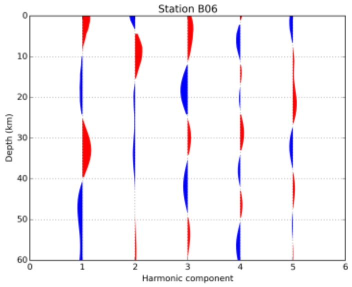

Station B08:

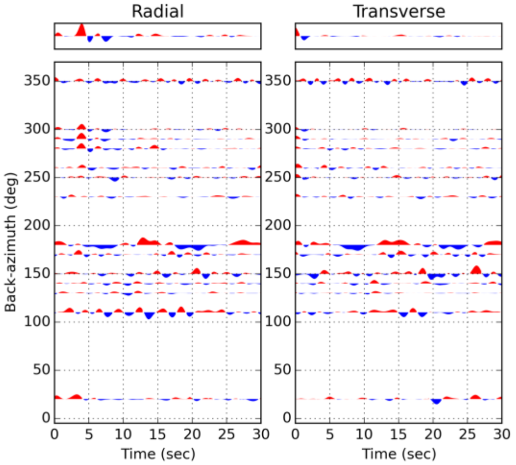

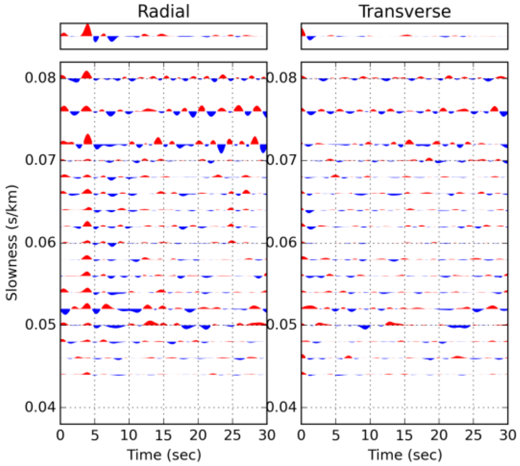

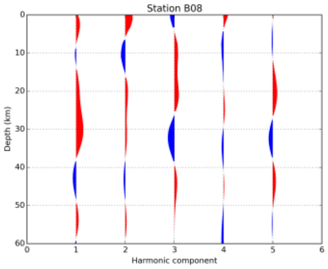

Station B09:

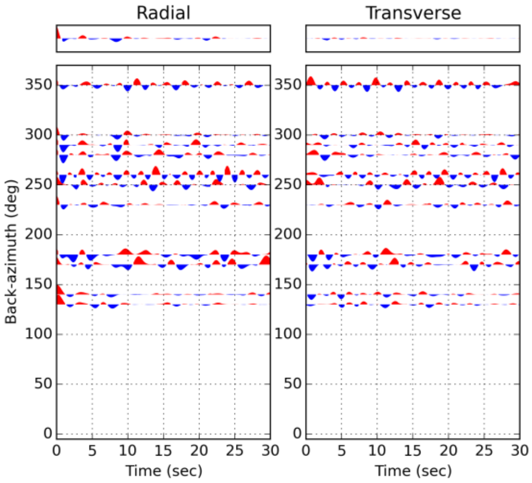

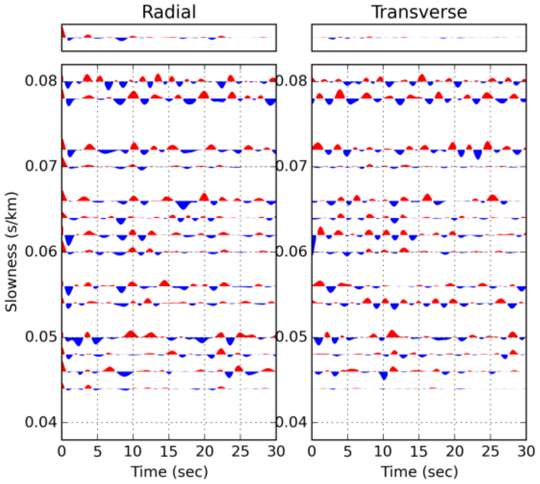

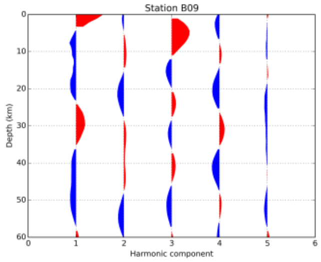

Station B11:

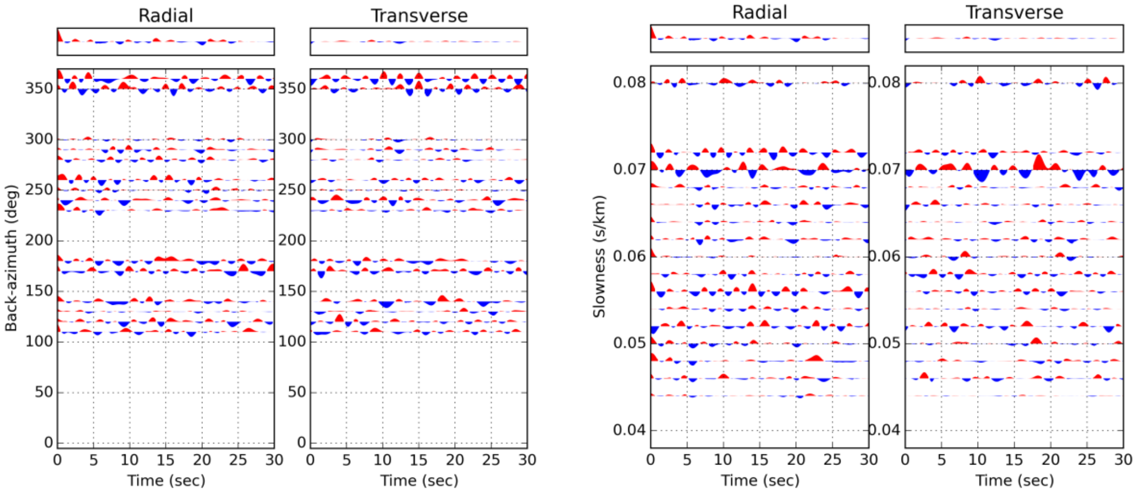

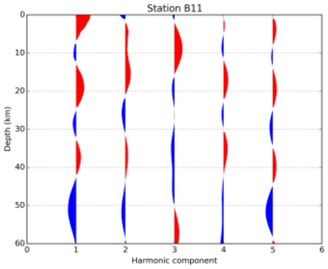

Station B12:

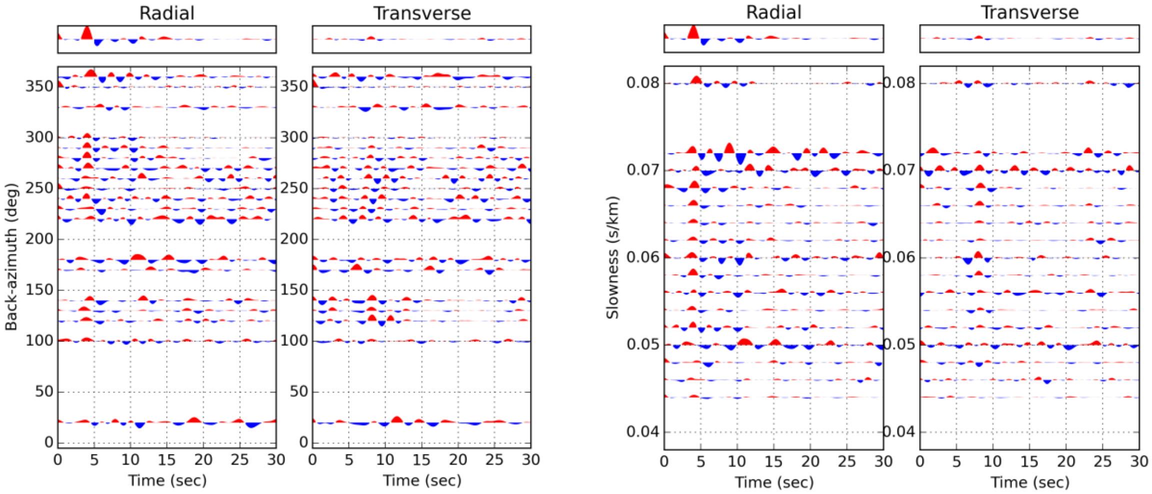

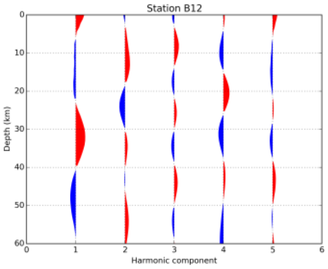

Station B13:

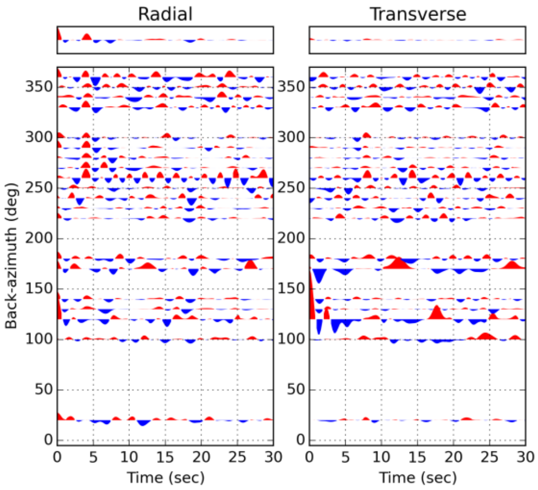

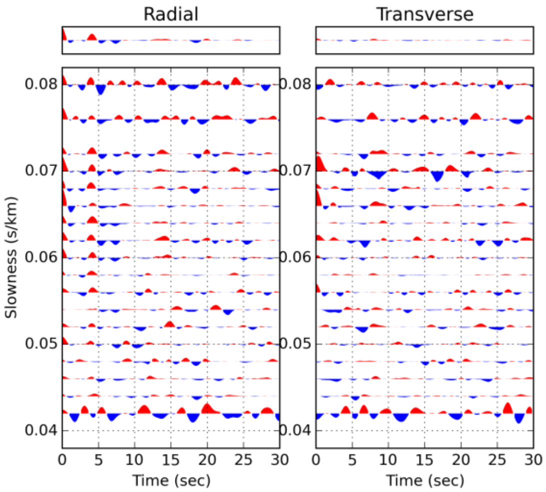

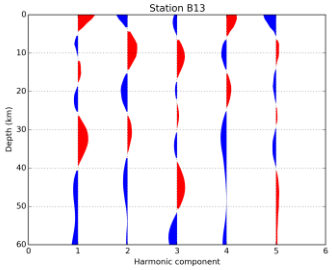

Station B15: